frontiers | Frontiers in Astronomy and Space Sciences

TYPE Review
PUBLISHED 24 December 2024
DOI 10.3389/fspas.2024.1422341

OPEN ACCESS

EDITED BY
David Knudsen,
University of Calgary, Canada

REVIEWED BY
Vladimir Krasnoselskikh,
UMR7328 Laboratoire de Physique et Chimie de l'Environnement et de l'Espace (LPC2E), France
R. S. Pandey,
Amity University, India

*CORRESPONDENCE
M. W. Dunlop,
malcolm.dunlop@stfc.ac.uk

RECEIVED 23 April 2024
ACCEPTED 05 December 2024
PUBLISHED 24 December 2024

CITATION
Dunlop MW, Fu H-S, Shen C, Tan X, Dong X-C, Yang Y-Y, Robert P and Escoubet CP (2024) Curlometer and gradient techniques: past and future applications.
Front. Astron. Space Sci. 11:1422341.
doi: 10.3389/fspas.2024.1422341

Curlometer and gradient techniques: past and future applications

M. W. Dunlop[1,2]*, H.-S. Fu[1], C. Shen[3], X. Tan[1], X.-C. Dong[4], Y.-Y. Yang[5], P. Robert[6] and C. P. Escoubet[7]

[1]School of Space and Earth Sciences, Beihang University, Beijing, China, [2]Rutherford Appleton Laboratory Space, Science and Technology Facilities Council, Didcot, United Kingdom, [3]School of Science, Harbin Institute of Technology, Shenzhen, China, [4]Department of Geophysics, Yunnan University, Kumning, China, [5]National Institute of Natural Hazards, Ministry of Emergency Management of China, Beijing, China, [6]Laboratoire de Physique des Plasmas, Ecole Polytechnique, Palaiseau, France, [7]European Space Agency/European Space Research and Technology Centre, Noordwijk, Netherlands

We review the range of applications and use of multi spacecraft techniques, applicable to close formation arrays of spacecraft, focusing on spatial gradient based methods, and the curlometer in particular. The curlometer was originally applied to Cluster multi-spacecraft magnetic field data, but later was updated for different environments and measurement constraints such as the NASA MMS mission, small-scale formation of 4 spacecraft; the 3 spacecraft configurations of the NASA THEMIS mision, and derived 2-4 point measurements from the ESA Swarm mission. In general, spatial gradient based methods are adaptable to a range of multi-point and multi-scale arrays. We also review the range of other techniques based on the computation of magnetic field gradients and magnetic field topology in general, including: magnetic rotation analysis and various least squares approaches. We review Taylor expansion methodology (FOTE), in particular, which has also been applied to both Cluster and MMS constellations, as well as interpretation of simulations. Four-point estimates of magnetic gradients are limited by uncertainties in spacecraft separations and the magnetic field, as well as the presence of non-linear gradients and temporal evolution. Nevertheless, the techniques can be reliable in many magnetospheric regions where time stationarity is largely applicable, or when properties of the morphology can be assumed (for example, the expected orientation of underlying large-scale structure). Many magnetospheric regions have been investigated directly (illustrated here by the magnetopause, ring current and field-aligned currents at high and low altitudes), and options for variable numbers of spacecraft have been considered. The comparative use of plasma measurements and possible new methodology for arrays of spacecraft greater than four are also considered briefly.

KEYWORDS

curlometer analysis, multi-spacecraft, analysis methods, magnetosphere, magnetic gradients and reconstruction

1 Introduction

The four Cluster II spacecraft (Escoubet et al., 2001) allowed 3-D structure and temporal evolution to be probed through the development of multi-spacecraft techniques for the first

time. These techniques specifically allow spatial gradients of key quantities to be analyzed, typically through first order approximations, or Taylor expansion around measurement points (e.g., Fu et al., 2015). Such analysis was first described in a book on collected multi-spacecraft analysis techniques in 1998 (Paschmann and Daly, 1998). The application of these multi-spacecraft methods was updated in (Paschmann and Daly, 2008), where here we focus on magnetic gradients and specifically magnetic currents (e.g., Dunlop and Eastwood, 2008; Shen and Dunlop, 2008; Vogt et al., 2008). The operation of Cluster provided a spacecraft configuration which maintained a quasi-tetrahedral formation for much of its life and Cluster is still the only space physics mission to provide fully four-point coverage over a large spatial range of scales; over a time epoch of two solar cycles (see Dunlop et al., 2021b; Escoubet et al., 2021).

The methodology, covering a wide range of analysis techniques, has been continuously developed to determine key quantities and investigate a large number of phenomena and has been applied to other missions in the 22 years since then (such as MMS, THEMIS and Swarm). The Magnetospheric Multi-Scale (MMS) mission maintained a close four spacecraft configuration on smaller separation scales (a few *km*) than Cluster for much of its orbit (Burch et al., 2016), while during extended operations (Angelopoulos, 2008), some of the NASA THEMIS spacecraft flew in a 3-spacecraft configuration in the magnetosphere and the ESA Swarm low orbit (LEO) polar mission provided both 2 and 3 spacecraft measurements in close formations (Friis-Christensen et al., 2008) on meso-scales (~100 *km*).

The future interest in multi-spacecraft methods remains strong; particularly in their development to make best use of planned larger arrays of spacecraft capable of probing multiscale phenomena, e.g., Plasma Observatory (Retinò et al., 2022), AME (Dai et al., 2020) and Helioswarm (Klein et al., 2023).

2 The curlometer and basic concepts

2.1 Integral method

The application of the curlometer to Cluster data was reviewed by Dunlop and Eastwood (2008). More recently, its adaption to the context of the high altitude ionosphere, focusing on the determination of field-aligned currents (FAC) was covered by Dunlop et al. (2020) and Trenchi et al. (2020) [see other papers in the ISSI book on ionospheric multi-spacecraft data analysis tools (Dunlop and Lühr, 2020)]. The method has also been reviewed by (Dunlop et al., 2018; Dunlop et al., 2021a; Dunlop et al., 2021b), and was surveyed by Robert and Dunlop (2022), and its application to the Earth's ring current region has also been recently analysed in the context of MMS data (Tan et al., 2023), who also addressed its accuracy in different regimes. The Cluster Science archive (http://www.cosmos.esa.int/web/csa/software) contains method implementations also in the technical note by Middleton and Masson (2016).

The calculation uses the integral form of Ampère's law, i.e., $\mu_0 \boldsymbol{J} = \mathbf{curl}(\boldsymbol{B})$ neglecting the displacement current ($\mu_0 \varepsilon_0 \partial \boldsymbol{E}/\partial t$) for high electrical conductivity (Russell et al., 2016), where $\boldsymbol{B}$ and $\boldsymbol{E}$ are the magnetic and electric fields and $\boldsymbol{J}$ is the current density. The technique (Dunlop et al., 1988; Robert et al., 1998a) combines four, non-planar spatial positions to make a linear estimate of the electric current density, i.e., $\mu_0 <\boldsymbol{J}> .\left(\Delta \boldsymbol{R}_i \Delta \boldsymbol{R}_j\right) = \Delta \boldsymbol{B}_i . \Delta \boldsymbol{R}_j - \Delta \boldsymbol{B}_j . \Delta \boldsymbol{R}_i$, where $\Delta \boldsymbol{B}_i$, $\Delta \boldsymbol{R}_i$ are the differences in the measured magnetic field at positions (i, j) to a reference spacecraft, giving a rugged and simple formalism (see also Section 2.2). The current density normal to each face of the spacecraft tetrahedral configuration is represented by the terms on the left-hand side of the equation. One of the four normal components is redundant and can be used to check stability of the estimate (Dunlop et al., 2018; Dunlop et al., 2020), by choosing different faces in the estimate of $\boldsymbol{J}$. For irregular spacecraft configurations, this also allows some flexibility to choose which face gives the best estimate of a component, where the relative alignment of the spacecraft configuration to the local field geometry is significant and often only one face determines a stable $\boldsymbol{J}$ component (see also the methodology in Vogt et al., 2009; Shen et al., 2012b).

A partial estimate of one component can still provide useful information if the large-scale current orientation is assumed, such as for FACs and in the case of the *in situ* ring current, where the azimuth component is significant (Zhang et al., 2011). For example, the three magnetospheric THEMIS spacecraft (Yang et al., 2016) can be used as shown in the left panel of Figure 1 in the ring current, but these assumptions can severely limit the stability of the estimates (Tan et al., 2023), and indeed the need to project the normal component into the ring plane means assumptions on the form of the large-scale currents are critical. The right-hand panel in Figure 1, illustrates that Swarm close configurations can also be used for partial and full current estimates with assumptions on the stationarity of the currents (over a few seconds) and that the field-aligned component is dominant or force-free (Shen et al., 2012a; Ritter et al., 2013; Vogt et al., 2013; Dunlop et al., 2015b, references in Dunlop and Lühr, 2020).

The right-hand side of Figure 1 illustrates the adaption in Dunlop et al. (2015b), where adjacent positions are used to form at least four points in space. As with the standard form of the curlometer, the convection time across the array is the relevant temporal scale for the estimates. In the case of Swarm this is typically 5–10 s for separation scales of around 100–150 km for the Swarm A,C pair of spacecraft, which fly side by side in near circular, polar orbits (~500 km altitude). Swarm B flies at a slightly higher altitude in an orbit but is only in alignment at specific times during the mission. In the special close configuration shown in Figure 1, a series of values can be made from different combinations of the five points (A,B,C,A',C'), providing information on any temporal changes as well as comparative estimates. For resolving the FAC component ACA'C' provides a vertical component of J (Ritter et al., 2013). The configuration ABC provides simultaneous measurements, but suffers from the fact that the plane is not well aligned to the FACs.

Although generally robust, the relative structure scales applying affect the validity range of the estimates. For Cluster separations (>100 km), the dominant error arises from nonlinear gradients, while at MMS separations (~5–10 km) measurement uncertainties can be important [typically these affect the estimate below a threshold |J| (Dunlop et al., 2018), i.e., for the small MMS tetrahedron scales (a few km), measurement uncertainty (~0.1 nT in B; ~100 m for R and millisecond timing) drives the error unless the current density is greater than several nAm^{-2}]. Both Runov et al. (2005) and Forsyth et al. (2011), for example, have examined the effect of the characteristic scale of current structures

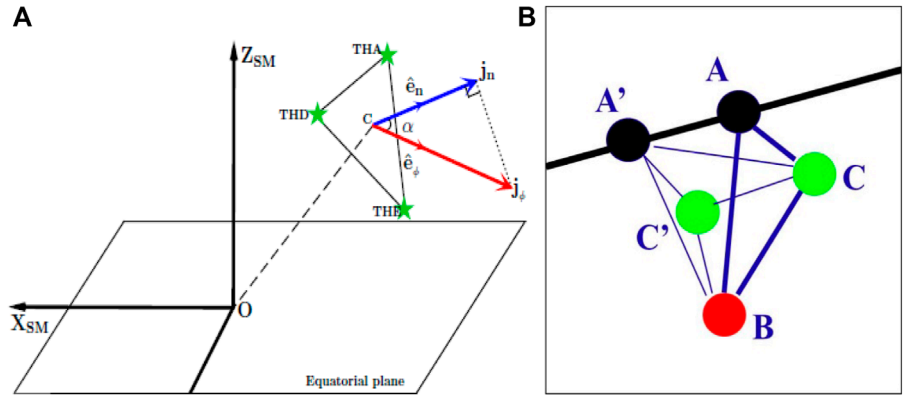

FIGURE 1
A configuration of the three THEMIS spacecraft in the ring current [from Yang et al. (2016), **(A)**], where the current density normal to the THEMIS plane can be projected into Jϕ direction as shown, and a configuration of the three Swarm spacecraft (A,B,C) with adjacent positions (A',C') taken from a few seconds earlier **(B)**.

on the use of quality estimates and indeed Tan et al. (2023) have compared MMS to Cluster results, which sample on distinct large and small spatial scales in the ring current. The linear estimator Q = |divB|/|curl(B)| has been used extensively as an indirect quality parameter (Robert et al., 1998a; Haaland et al., 2004b), along with the constellation shape (elongation and planarity) as discussed in more detail in Section 2.2. The linear estimate of the average value of divB over the volume of the tetrahedron is an integral part of the method and is given by $<div(\boldsymbol{B})> \left|\Delta \boldsymbol{R}_i.\Delta \boldsymbol{R}_{\hat{j}}\Delta \boldsymbol{R}_k\right| = \left|\sum_{cyclic}\Delta \boldsymbol{B}_i.\Delta \boldsymbol{R}_{\hat{j}}\Delta \boldsymbol{R}_k\right|$,

$$\text{e.g. } <div(\boldsymbol{B})>_{1234}\left(\Delta \boldsymbol{R}_{12}\cdot\Delta \boldsymbol{R}_{13}\wedge\Delta \boldsymbol{R}_{14}\right) = \Delta \boldsymbol{B}_{12}\cdot\Delta \boldsymbol{R}_{13}\wedge\Delta \boldsymbol{R}_{14} + \Delta \boldsymbol{B}_{13}\cdot \Delta \boldsymbol{R}_{14}\wedge\Delta \boldsymbol{R}_{12} + \Delta \boldsymbol{B}_{14}\cdot\Delta \boldsymbol{R}_{12}\wedge\Delta \boldsymbol{R}_{13}.$$

This full combination of the four positions are needed for Q to be used which is found unreliable if the spacecraft configuration is highly irregular and not well aligned to the background magnetic field structure. The estimate of Q has also been used in qualification of the FOTE (First-Order Taylor Expansion) method (see Section 2.3).

In the magnetosphere, the effect of dipole non-linear gradients, not associated with current density [first noted in Dunlop et al. (2002), while Grimald et al. (2012) considered this in the context of the ring current], can be minimised by subtracting the dipole (or IGRF) field from the measured magnetic field to give magnetic residuals, e.g., for studies of the *in situ* ring current (Yang et al., 2016), where dipole gradients are significant and at low altitude orbits (LEO) where the formation of magnetic residuals is normal practice, particularly for Swarm (Ritter et al., 2013; Dunlop et al., 2020).

2.2 The influence of elongation, planarity and Q: the limiting case

At the mesoscales of Cluster separations, the accuracy of the curlometer estimate primarily depends on how the neglected non-linear gradients contribute in the context of the spacecraft constellation, i.e., its scale, shape (irregularity) and relative orientation to the measured current structure. This is also true at smaller separation scales (e.g., for MMS) but then measurement errors (in the magnetic field, position and timing) also become significant. For Cluster, therefore, the spatial sampling through the constellation shape was considered. To characterize the shape using the three eigenvalues of the volumetric tensor **R** are $\mathbf{W}_1$, $\mathbf{W}_2$, $\mathbf{W}_3$ (in order of magnitude, i.e., $\mathbf{W}_1 > \mathbf{W}_2 > \mathbf{W}_3$) the square roots a, b, and c are used to define: elongation $E = 1-(b/a)$ and planarity $P = 1-(c/b)$. These parameters can be used to check the degree of irregularity of the tetrahedral shape, so that they complement the value of Q, since this because a poor indicator for irregular tretrahedral shape.

In terms of the curlometer approximation, whether the method is used on three magnetospheric spacecraft from the THEMIS mission, or the tetrahedral constellations of MMS and Cluster, current density components are calculated starting from a single plane formed by 3 spacecraft. We therefore need to calculate, to first order, the closed integral (Equation 1) of the magnetic field and divide it by the area of the triangle formed by 3 spacecraft (see also discussion of the integral forms in Section 2.3).

$$\mu_0 J_{av} = \frac{\oint \vec{B}\bullet d\vec{s}}{S} \tag{1}$$

Under the condition of limited observation data, we calculate the integral of the magnetic field, and the area of the triangle formed by three positions, from the following Equations 2, 3 (as written above in condensed notation).

$$\oint_{123}\vec{B}\bullet d\vec{s} \approx \left(\frac{\vec{B_1}+\vec{B_2}}{2}\right)\bullet(\vec{r_2}-\vec{r_1}) + \left(\frac{\vec{B_2}+\vec{B_3}}{2}\right)\bullet(\vec{r_3}-\vec{r_2}) + \left(\frac{\vec{B_3}+\vec{B_1}}{2}\right)\bullet(\vec{r_1}-\vec{r_3}) \tag{2}$$

$$S_{123} = \left|\frac{(\vec{r_2}-\vec{r_1})\times(\vec{r_3}-\vec{r_1})}{2}\right| = \left|\frac{(\vec{r_3}-\vec{r_{21}})\times(\vec{r_1}-\vec{r_2})}{2}\right| = \left|\frac{(\vec{r_1}-\vec{r_3})\times(\vec{r_2}-\vec{r_3})}{2}\right| \tag{3}$$

In the limiting case, the three spacecraft are collinear. Suppose that spacecraft 3 is between 1 and 2, with a distance t from 1 and a distance 1-t from 2.

$$\vec{\boldsymbol{B}_3} = (1-t)\vec{\boldsymbol{B}_1} + t\vec{\boldsymbol{B}_2} + \vec{\Delta \boldsymbol{B}} \tag{4}$$

$$\left(\vec{\boldsymbol{r}_1} - \vec{\boldsymbol{r}_3}\right) = t\left(\vec{\boldsymbol{r}_1} - \vec{\boldsymbol{r}_2}\right) \tag{5}$$

$$\left(\vec{\boldsymbol{r}_3} - \vec{\boldsymbol{r}_2}\right) = (1-t)\left(\vec{\boldsymbol{r}_1} - \vec{\boldsymbol{r}_2}\right) \tag{6}$$

$\vec{\Delta \boldsymbol{B}}$ in Equation 4 is the non-linearity term, but it could have contributions from the nonlinearity of the magnetic field, measurement errors of magnetometer, differences between the measurement at each spacecraft and time-varying error introduced by time interpolation. Putting Equations 4–6 to Equation 2, we get Equation 7

$$\oint_{123} \vec{\boldsymbol{B}} \bullet d\vec{s} \approx \left(\vec{\Delta \boldsymbol{B}}/2\right) \bullet \left(\vec{\boldsymbol{r}_1} - \vec{\boldsymbol{r}_2}\right) \tag{7}$$

If $\vec{\Delta \boldsymbol{B}}$ is not zero, which is almost certain, then in this limiting case the integral of the magnetic field is not zero, while the area of the triangle formed by the three spacecraft is exactly zero; producing an infinite current error. Thus, when the 3 spacecraft are collinear, the actual current density cannot be obtained. Even if the three are not collinear, the calculated current density will increase dramatically as they approach the collinear position. Because of the nonlinear term, the area approaches zero faster than the curve integral approaches zero. Estimating accurate error is limited by the difficulty of obtaining the exact nonlinear term, however, future work will attempt to quantify this. It should also be noted that the parameter Q cannot be well used in this limit, because *curB* becomes infinite but not *divB*. Thus, Q will remain a very low value and lose its expected function. In past analysis, therefore, the Elongation for a triangle has been used to gain an empirical reliability and exclude bad results. In other words, only those calculation results meeting a certain Elongation condition (e.g., less than 0.8) can be trusted.

For the case of the full four spacecraft tetrahedral configurations (as for MMS and Cluster), a further step is needed as three current density components are obtained from three of the four planes in a tetrahedron. The current density vector is then obtained by solving equations (as indicated above). Using subscripts 1, 2, and 3 to represent the average current density J and the normal direction N of the three planes, respectively.

$$\begin{cases} N_{1x}J_x + N_{1y}J_y + N_{1z}J_z = J_1 \\ N_{2x}J_x + N_{2y}J_y + N_{2z}J_z = J_2 \\ N_{3x}J_x + N_{3y}J_y + N_{3z}J_z = J_3 \end{cases} \tag{8}$$

By denoting $N = \begin{bmatrix} N_{1x} & N_{1y} & N_{1z} \\ N_{2x} & N_{2y} & N_{2z} \\ N_{3x} & N_{3y} & N_{3z} \end{bmatrix}, J_{xyz} = \begin{bmatrix} J_x \\ J_y \\ J_z \end{bmatrix}, J_{123} = \begin{bmatrix} J_1 \\ J_2 \\ J_3 \end{bmatrix}$, then Equation 8 is reduced to Equation 9. And Jxyz is obtained (Equation 10).

$$NJ_{xyz} = J_{123} \tag{9}$$

$$J_{xyz} = N^{-1}J_{123} \tag{10}$$

The calculation process is actually naturally stable because of the closure of the equations for a sampled volume through Ampères law, and in addition the fourth face of the tetrahedron provides a check on the estimates. Nevertheless, if matrix N is not well-conditioned (i.e., ill-conditioned or near singular), we cannot get the true current (as will occur if the constellation is near planar). As mentioned earlier, the matrix N is made up of normal vectors on three planes, and the most likely (or perhaps the only) factor for poor quality is that some normal vectors are closely to be parallel. The effect on Q in this case is not well understood, but further work is expected to clarify this through specific analysis in the future. Currently, we can conservatively choose to trust the results obtained by the tetrahedral configuration with better non-coplanar conditions. This condition has been evaluated in the past through the added use of the Planarity, i.e., typically limiting this also below 0.8 (In practice, both parameters are combined into a quality index as the square route of the sum of the squares of E and P with this value <0.8, typically).

When using the curlometer method, careful attention to the configuration parameters of the constellation must be paid, therefore, due to the existence of these factors (arising from the neglected nonlinearity of the physical quantities). Tailored analysis of specific events can reduce the risk of calculation anomalies and in the case of large amounts of data can be statistically processed. Clearly, sampling by more spacecraft (and more than four spacecraft in particular) can help stabilize the estimate through alternative choice of the planes and by selection of particular tetrahedra within the constellation, but then the tracking of the more complex constellations requires more management. This and the use of the quality indicators, have been considered, for example, for new, proposed constellation mission operations, such as Plasma Observatory (Retinò et al., 2022) and Helioswarm (Klein et al., 2023).

2.3 Advanced integral theorems: geometrical approach

The curlometer method rests on the ability to estimate linear gradients in the measured quantities (specifically the magnetic field) between spacecraft positions. Apart from the linear interpolation method (Chanteur and Harvey, 1998) and the least-squares method (Harvey, 1998), the geometrical method (integral theorems), introduced above is the third way to obtain general estimators of the linear gradients of physical quantities. Recently, Shen and Dunlop (2023) have made full use of a geometrical method (summarized below in Equations 11–26) to derive the gradient, divergence, and curl of physical quantities with the integral theorems. Furthermore, this geometrical method has the special advantage to easily derive the field gradients for observations made by a planar constellation. The errors in the estimators of the linear gradients from the geometrical method were found to enter at second-order and it was illustrated that the method based on integral theorems are equivalent to the spatial interpolation method (Chanteur, 1998; Chanteur and Harvey, 1998; Vogt et al., 2009) and the least-squares method (Harvey, 1998; De Keyser, 2008; Hamrin et al., 2008) for deriving linear gradients.

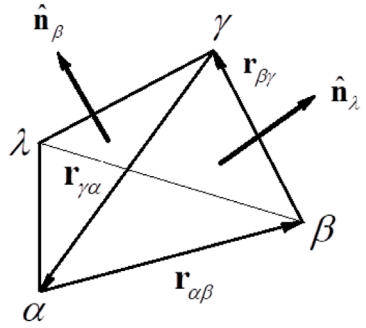

FIGURE 2
Demonstration of the constellation tetrahedron (Shen and Dunlop, 2023).

In Figure 2 the position vectors of the four spacecraft in a tetrahedral configuration are $\mathrm{r}_\alpha(\alpha = 1,2,3,4)$. The barycenter coordinates are chosen as $\mathbf{r}_c \equiv \frac{1}{N}\sum_{\alpha=1}^{N}\mathbf{r}_\alpha = 0$. The spacecraft α, β, and γ constitute a face triangle as discussed earlier $\Delta_{\alpha\beta\gamma}$, where the vertex opposite to this is λ, as shown in Figure 2. The three vertices α, β, and γ of the face $\Delta_{\alpha\beta\gamma}$ are defined to rotate anticlockwise around its normal $\hat{\mathbf{n}}_\lambda$. In this notation, the vector area of the face $\Delta_{\alpha\beta\gamma}$ of the tetrahedron is

$$\mathbf{S}_\lambda = \mathbf{S}_{\alpha\beta\gamma} = \frac{1}{2}\mathbf{r}_{\alpha\beta}\times\mathbf{r}_{\beta\gamma} = \frac{1}{2}\left|\mathbf{r}_{\alpha\beta}\times\mathbf{r}_{\beta\gamma}\right|\hat{\mathbf{n}}_\lambda \tag{11}$$

The volume of the tetrahedron is

$$V = -\frac{1}{6}r_{\beta\alpha}\cdot\left(r_{\beta\lambda}\times r_{\beta\gamma}\right) \tag{12}$$

For a certain arbitrary scalar field f, vector field $\mathbf{u}$ and tensor field $\mathbf{T}$, the αth satellite of the constellation yields the scalar field f_α, vector field $\mathbf{u}_\alpha$ and tensor field $\mathbf{T}_\alpha$. The scalar field f, vector field $\mathbf{u}$ and tensor field $\mathbf{T}$ obey the following integral theorems (Bittencourt, 2004):

$$\int_V \nabla f \mathrm{d}V = \oint_s f\mathrm{d}\mathbf{S} \tag{13}$$

$$\int_V \nabla\mathbf{u}\mathrm{d}V = \oint_S \mathrm{d}\mathbf{S}\,\mathbf{u} \tag{14}$$

$$\int_V \nabla\cdot\mathbf{u}dV = \oint_S \mathbf{u}\cdot d\mathbf{S} \tag{15}$$

$$\int_V \nabla\times\mathbf{u}dV = \oint_S d\mathbf{S}\times\mathbf{u} \tag{16}$$

$$\int_V \nabla\cdot\mathbf{T}\mathrm{d}V = \oint_S \mathrm{d}\mathbf{S}\cdot\mathbf{T} \tag{17}$$

Starting from these integral theorems, Shen and Dunlop (2023) have obtained the estimators of the gradients of a scalar field f, vector field $\mathbf{u}$ and tensor field $\mathbf{T}$, as well as the curl and divergence of the vector field $\mathbf{u}$, respectively, as below:

$$\langle\nabla f\rangle = -\frac{1}{3V}\sum_{\lambda=1}^{4} f_\lambda\mathbf{S}_\lambda \tag{18}$$

$$\langle\nabla\mathbf{u}\rangle = -\frac{1}{3V}\sum_{\lambda=1}^{4}\mathbf{S}_\lambda\mathbf{u}_\lambda \tag{19}$$

$$\langle\nabla\cdot\mathbf{T}\rangle = -\frac{1}{3V}\sum_{\lambda=1}^{4}\mathbf{S}_\lambda\cdot\mathbf{T}_\lambda \tag{20}$$

$$\langle\nabla\times\mathbf{u}\rangle = -\frac{1}{3V}\sum_{\lambda=1}^{4}\mathbf{S}_\lambda\times\mathbf{u}_\lambda \tag{21}$$

$$\langle\nabla\cdot\mathbf{u}\rangle = -\frac{1}{3V}\sum_{\lambda=1}^{4}\mathbf{S}_\lambda\cdot\mathbf{u}_\lambda \tag{22}$$

Considering the reciprocal vector $\mathbf{k}_\alpha$ as defined by Chanteur (1998)

$$\mathbf{k}_\alpha = \frac{\mathbf{r}_{\beta\lambda}\times\mathbf{r}_{\beta\gamma}}{\mathbf{r}_{\beta\alpha}\cdot\left(\mathbf{r}_{\beta\lambda}\times\mathbf{r}_{\beta\gamma}\right)} = -\frac{1}{3V}\mathbf{S}_\alpha \tag{23}$$

then the above estimators are identical to those from the interpolation method (Chanteur, 1998).

The integral theorems method, however, has one special advantage, it can easily derive the field gradients for measurements from a planar constellation [e.g., as for the three-spacecraft THEMIS (Friis-Christensen et al., 2006) or Swarm (Angelopoulos, 2009) configurations].

By using the following integral theorem applied to the triangle $\Delta_{\alpha\beta\gamma}$:

$$\oint_C \phi d\mathbf{l} = \int_S d\mathbf{S}\times\nabla\phi \tag{24}$$

the averaged gradient of the scalar field in the plane of the constellation is readily derived as the following formula (Shen and Dunlop, 2023)

$$\langle\nabla\phi\rangle_\perp = -\frac{1}{2S_{\alpha\beta\gamma}}\phi_{\{\alpha}\mathbf{r}_{\beta\gamma\}}\times\hat{\mathbf{n}} \tag{25}$$

Similarly, for a vector field $\mathbf{u}$, its averaged gradient of the scalar field in the plane of the constellation is

$$\langle\nabla\mathbf{u}\rangle_\perp = -\frac{1}{2S_{\alpha\beta\gamma}}\mathbf{u}_{\{\alpha}\mathbf{r}_{\beta\gamma\}}\times\hat{\mathbf{n}} \tag{26}$$

A rigid error analysis has been made for this geometric approach based on Taylor expansion (Shen and Dunlop, 2023). It is verified that the truncation error of the method is at the order of $(L/D)^2$, where L is the characteristic size of the constellation tetrahedron (Robert et al., 1998b) and D is the length scale of the field structure measured. It is found that the truncation error for deriving the linear gradient with the four point measurements by Cluster and MMS is actually very small and Cluster (Escoubet et al., 1997; Escoubet et al., 2001), THEMIS (Angelopoulos, 2009) and MMS (Burch et al., 2016) are generally able to yield stable estimates of current density, charge density, curvature of magnetic field lines, and other related parameters (Shen et al., 2003; Haaland et al., 2021; Pitout and Bogdanova, 2021; Shen et al., 2021b; Robert and Dunlop, 2022).

3 Magnetic gradients and topology

The gradient and curvature terms in the dyadic of the magnetic field, B, can be linearly estimated (Chanteur, 1998; Harvey, 1998; Shen and Dunlop, 2008; Vogt et al., 2008; Shen et al., 2012a; Shen et al., 2012b), from which the current density can be obtained.

Key methodology includes magnetic curvature and rotation analysis (Shen et al., 2007; Shen et al., 2012a); least squares analysis of planar reciprocal vectors (De Keyser et al., 2007; Hamrin et al., 2008; Vogt et al., 2009; Vogt et al., 2013), and a range of techniques related to Taylor expansion around the measurement points (FOTE method, see Section 3.3). Estimates based on these gradient methods basically depend on both the integrity of the spacecraft array and stationary properties (temporal dependence) of the magnetic structures, although additional constraints or assumptions can be incorporated. More recently, the polynomial reconstruction of the magnetic field topology has been explored using MMS data by Denton et al. (2020), Denton et al. (2022).

3.1 Magnetic rotation analysis applications

In addition to estimating direct gradients, Magnetic Curvature Analysis (MCA) (Shen et al., 2003) and Magnetic Rotation Analysis (MRA) (Shen et al., 2007) give the 3-D topology of the magnetic field (curvature radius, normal direction and binormal direction of the magnetic field-lines). Particular results have been obtained in the magnetotail current sheet (Shen et al., 2008a; Shen et al., 2008b; Rong et al., 2011); the Earth's ring current (Shen et al., 2014); flux ropes and plasmoids (Zhang et al., 2013; Yang et al., 2014); reconnection regions (Lavraud et al., 2016; Zhang et al., 2016), and in the cusp and at the magnetopause (Shen et al., 2011; Xiao et al., 2018).

The curvature of field-lines (from MCA) from Cluster located within the ring current are shown on the left-hand side of Figure 3, which indicates current strength in a complimentary manner to the magnetic gradient based J calculation. The plot shows a decrease in relative curvature, which implies a growth of the implied current density which is related to increasing geomagnetic activity (e.g., SYM-H). There is also a dawn-dusk asymmetry, which is most apparent at lower activity levels. The right-hand side of Figure 3 shows that the method can resolve the form of the tail current sheet in terms of different current sheet geometry. As discussed by Rong et al. (2011) these can be classified as: normal, flattened and tilted. These distinct geometries result from the combined MCA/MRA methodology, where the key properties of curvature radius, normal direction and binormal direction are extracted to inform the sheet characteristics controlling current sheet dynamics.

3.2 Least-squares methods for multi-point gradient computation

Typically, instruments record multiple data points in the convection time needed to cover a comparable distance to the separation scales, which in principle carry information relevant for calculation of the gradient, as was already noted by Harvey (1998). This is particularly true if a certain degree of time invariance in the structures of interest can be assumed. The Gradient Analysis by Least-Squares (GALS) technique (Hamrin et al., 2008) and the Least-Squares Gradient Calculation (LSGC) technique (De Keyser et al., 2007; De Keyser, 2008) apply these ideas. The latter is based on least squares gradient calculation by approximating the measured quantity (scalar or vector) through Taylor series expansion around the measurement reference point (typically the barycenter). This expansion describes the magnetic field, for example, its spatial and temporal gradients and non-linear terms at higher-order. An assumption that the gradients are constant on certain spatial scales, allows higher-order terms to be estimated. It follows that, in practice, an iterative, weighted least-squares, procedure can be devised.

The method can provide error estimates on the results. As in the case of the curlometer, these reflect errors in both the measurement and non-linear behaviour, (to simplify, uncorrelated measurement errors as well as homogeneity parameters can be assumed for all three components). The property that divB = 0, that the parallel magnetic field gradient is zero, or static structures can be added as constraints. An important application of a higher number of spacecraft is in error control. Although other numbers of measurement points can be used, quality of the results depends on the measurement errors.

It is worth also noting here that the conventional ways to calculate the gradient involve the calculating of the inverse of volume tensor (e.g., Chanteur, 1998; Harvey, 1998; Shen et al., 2003; Shen et al., 2007). The volume tensor would become an ill-conditioned matrix, however, when Cluster tetrahedron becomes an irregular shape, e.g., plane-like or line-like, so that the direct calculation of the inverse of volume tensor would yield significant error and gradient cannot be correctly calculated in this case.

Shen et al. (2012b) avoided the problem of irregular shaped configurations of spacecraft, by introducing a procedure where transforming coordinates into the eigenvector space of volume tensor allows the gradient to be universally calculated. The gradient calculation can involve the inverse of volume tensor (e.g., Chanteur, 1998; Harvey, 1998; Shen et al., 2003; Shen et al., 2007), which is problematic for very irregular shapes. A bonus of the approach of Shen et al. (2012b) is that it can be applied to three-point magnetic field observations (e.g., as in the case of THEMIS), to give current density and the vorticity of plasma flow, and to three-point plasma measurement for the vorticity of K-H waves (as for Cluster).

3.3 FOTE methods and applications: local Taylor expansion

The FOTE method is based on the Jacobian matrix δB, which is a 3 × 3 real matrix $\delta B_{ij} = \partial B_i/\partial r_j$. With four-point measurements of magnetic fields, ∂B_i and ∂r_j can be easily obtained. Theoretically, such matrix has three eigenvectors, e_1, e_2, e_3, and correspondingly three eigenvalues, λ_1, λ_2, λ_3. The sum of these three eigenvalues is zero ($\lambda 1+\lambda 2+\lambda 3 \equiv \nabla \cdot B = 0$), because the magnetic field is "non-divergent." This implies that either all the eigenvalues are real or one is real while the two others are conjugate complex (Fu et al., 2015; Fu et al., 2020).

The immediate application of the FOTE method is to find magnetic nulls (particularly in regions containing magnetic reconnection X-lines); complementing the analysis based on the use of the Poincare index (Xiao et al., 2006; Xiao et al., 2007) and field line reconstruction methods (He et al., 2008a; He et al.,

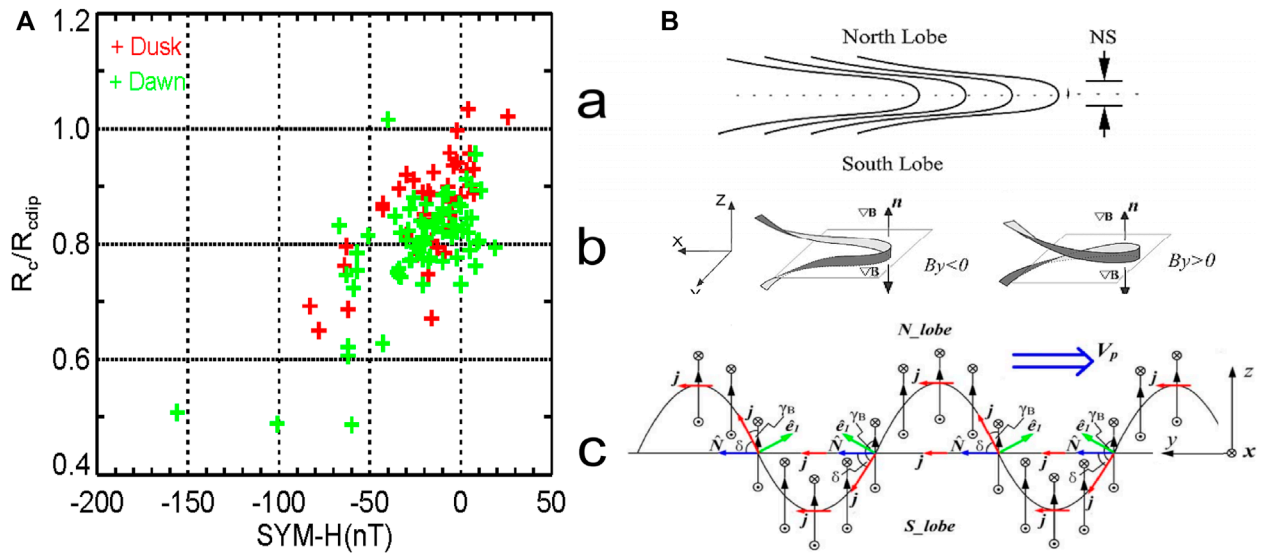

FIGURE 3
(A) Field-line curvature relative to that of the model dipole field for a set of ring current crossings sampled by Cluster (Shen et al., 2014), where dusk and dawn locations have different colours. **(B)** Cartoon of the types of field topology (Rong et al., 2011) found in the cross tail current sheet: (a) normal current sheet, (b) flattened current sheet (c) tilted current sheet (after Dunlop et al., 2021a).

2008b; Dunlop et al., 2009). Assuming that the magnetic field changes linearly around the spacecraft tetrahedron, the position of a magnetic null can be resolved if we perform the first-order Taylor expansion of magnetic fields around this null, $\mathbf{B}(\mathbf{r}) = \delta\mathbf{B}\cdot(\mathbf{r}-\mathbf{r}_0)$, where r_0 is the spacecraft position, r is the distance from spacecraft to the null, and B(r) is the magnetic field measured by each spacecraft. Applying the four-spacecraft measurements to this equation, r is easily resolved, and therefore, the null position is known (Fu et al., 2015). Notice that the null-spacecraft distance is a three-dimensional vector. Such distance, however, may involve uncertainties if the null is a quasi-2D structure (e.g., X-null). In other words, if the null is 2-D, the derived null-spacecraft distance in the "out-of-plane" direction is unreliable (Fu et al., 2019). In such situation, we only consider the 2-D null-spacecraft distance, i.e., the null-spacecraft distance in the reconnection plane.

Magnetic null types can also be identified. Since the sum of the three eigenvalues is zero ($\lambda_1+\lambda_2+\lambda_3 \equiv \nabla\cdot\mathbf{B}=0$), either all the eigenvalues are real or at least one is real and the other two are conjugate and complex. The different conditions affect the type of null: it is radial when the eigenvalues are real for both A- and B-type. A combination of one positive and two negative eigenvalues gives an A-type null, while two positive and one negative eigenvalue gives a B-type. In the other case, where only one eigenvalue is real, the null is an As- and Bs-type spiral (the As null corresponds to a positive real eigenvalue and the Bs null to a negative real eigenvalue). Sometimes large instrument uncertainties or magnetic field non-linearity mean the type cannot be identified, so is labelled "unknown". A, B, As, and Bs are all the null types in 3D regime. They are labeled by using the symbols △, ▷, ▲, ►, respectively (Fu et al., 2015; Fu et al., 2020).

The FOTE method can also determine the dimensionality of a magnetic null. Among the three eigenvalues of the Jacobian matrix, if one eigenvalue is significantly smaller than the two others, the three-dimensional A- and B-null will degenerate into two-dimensional X-null, or in other words, the magnetic topology will have a 2-D appearance; if the real part is significantly smaller than the imaginary part, the three-dimensional As- and Bs-null will degenerate into two-dimensional O-null, which certainly has the 2-D appearance (Fu et al., 2015; Wang et al., 2020). Typically, in spacecraft measurements, we simplify A and B nulls to X null if the three eigenvalues satisfy $\min(|\lambda|) < \frac{1}{4}\cdot\max(|\lambda|)$ and simplify As and Bs nulls to O null if the real and imaginary parts of the three eigenvalues satisfy $\max(|\mathrm{Real}(\lambda)|) < \frac{1}{4}\cdot\min(|\mathrm{Imag}(\lambda)|)$. The A, B, As, and Bs nulls are 3-D structures, while the X and O nulls are 2-D structures. Such 2-D structures are characterized by negligible magnetic fields in the "out-of-plane" direction. In space plasmas, the O null (or O line) is referred to plasmoid or flux rope. Figure 4 shows an example for the application of the FOTE method to find magnetic nulls during 12 magnetic-reconnection events detected by the MMS mission at the Earth's magnetopause, with the null-spacecraft distance (see the left-side vertical axis), null types (see the symbols), null dimensionality (see the labeling system at the bottom of the figure), and the analysis error (see the gray shade and the right-side vertical axis) exhibited (adapted from Fu et al., 2019).

During periods of magnetic reconnection, the open angle of separatrix-lines can be resolved by the method. The Jacobian matrix δB has three eigenvectors, e_1, e_2, e_3, and correspondingly three eigenvalues, $\lambda_1, \lambda_2, \lambda_3$. The open angle of two separatrix-lines is determined by the two eigenvectors related to the two large eigenvalues. The angle between these two eigenvectors is the open angle of the two separatrix-lines (Chen et al., 2018). For example, if $\lambda_1 > \lambda_2 > \lambda_3$, the open angle is the angle between e_1 and e_2. Such an open angle directly determines the reconnection rate of a reconnection process (Chen et al., 2019; Wang et al., 2020). Figure 5 is an example, showing the

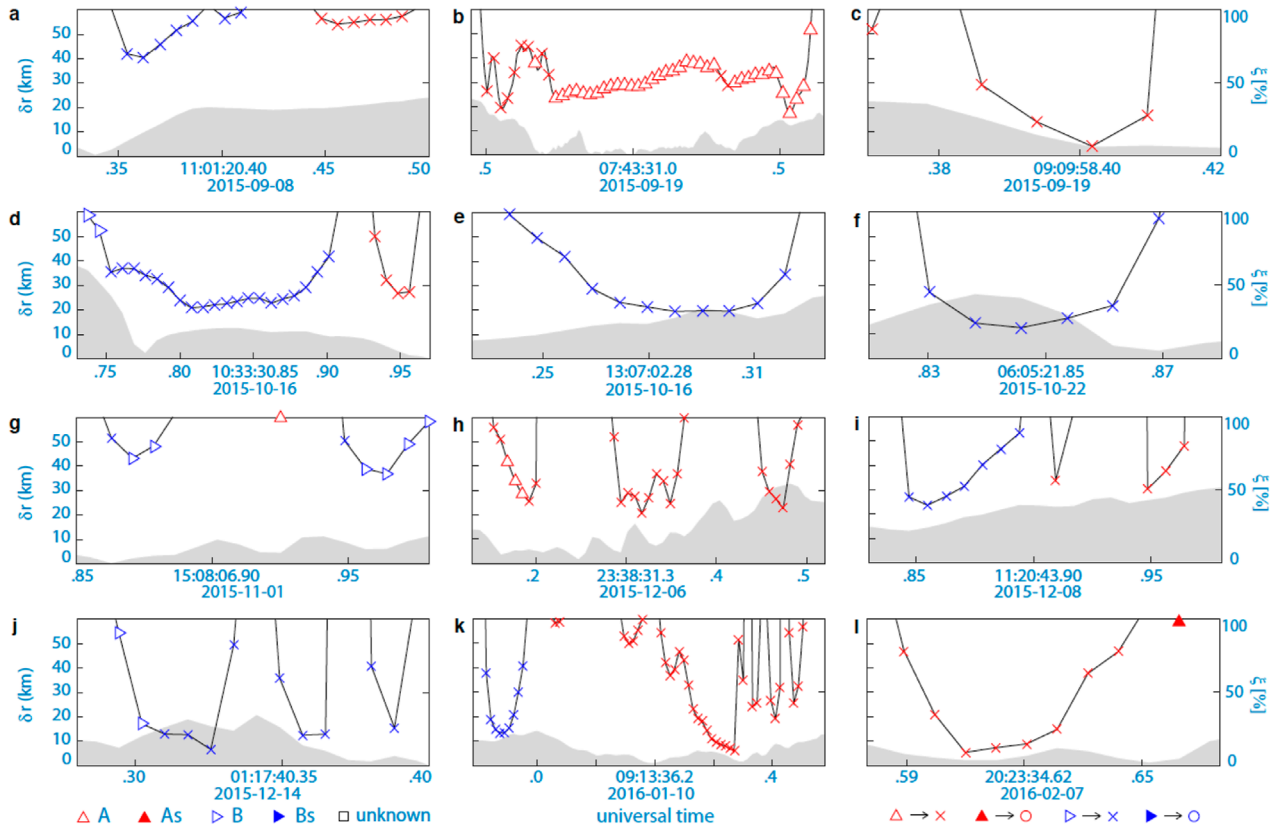

FIGURE 4
An example illustrating the application of the FOTE method to find magnetic nulls during 12 reconnection events **(A–L)** at the Earth's magnetopause (after Fu et al., 2019).

application of the FOTE method to resolve the open angle of separatrix-lines and deduce the reconnection rate during an unsteady reconnection at the Earth's magnetopause (adapted from Wang et al., 2020).

The FOTE method can be used in the reconstruction of magnetic topology around magnetic nulls. In eigenvector coordinates $e_1e_2e_3$, we trace and inverse-trace a few points around the null to obtain the magnetic field topology. The step length of trace/inverse-trace is typically set to be the local magnetic strength (Fu et al., 2016). Figure 6 illustrate the application of the FOTE method to reconstruct the topology of a radial-type magnetic null and a spiral-type magnetic null, which is also referred to the magnetic flux rope in spacecraft observations (modified from Fu et al., 2017; Wang Z. et al., 2019).

Finally, in terms of the errors during applications of the method to real data, we require the null-spacecraft distance to be less than the local ion inertial length, in order to guarantee that the null positions are accurately resolved. In addition, to guarantee that the null properties are accurately identified, we define two parameters ($\eta \equiv |\nabla \cdot \mathbf{B}|/|\nabla \times \mathbf{B}|$ and $\xi \equiv |(\lambda_1+\lambda_2+\lambda_3)|/|\lambda|_{max}$) and require them to be smaller than 0.4. These criteria are derived from the comprehensive test of three-dimensional simulation data (Fu et al., 2015; Fu et al., 2016).

4 Application of the curlometer to currents in the magnetosphere

Due to its robust and flexible nature, the curlometer calculation is perhaps the most widely used in the magnetosphere (notably applied in: the magnetopause boundary layer (Dunlop et al., 2002; Haaland et al., 2004a, e.g., Dunlop and Balogh, 2005; Panov et al., 2006; Panov et al., 2008; Shi et al., 2019); the magnetotail (Runov et al., 2006, e.g., Nakamura et al., 2008; Narita et al., 2013); the ring current (Vallat et al., 2005; Zhang et al., 2011, e.g., Shen et al., 2014; Yang et al., 2016); field-aligned currents (e.g., Forsyth et al., 2008; Marchaudon et al., 2009; Shi et al., 2010; Shi et al., 2012; Dunlop and Lühr, 2020) and other transient signatures and in the solar wind (e.g., Eastwood et al., 2002; Xiao et al., 2004; Shen et al., 2008a; Roux et al., 2015). Some of these applications are briefly reviewed here.

4.1 Basic use of the curlometer and time stationarity

The magnetopause boundary layer (MPBL) matched well the scale size of the early Cluster mission phases (100–2,000 km spacecraft separation). Figure 7 shows examples from Haaland et al.

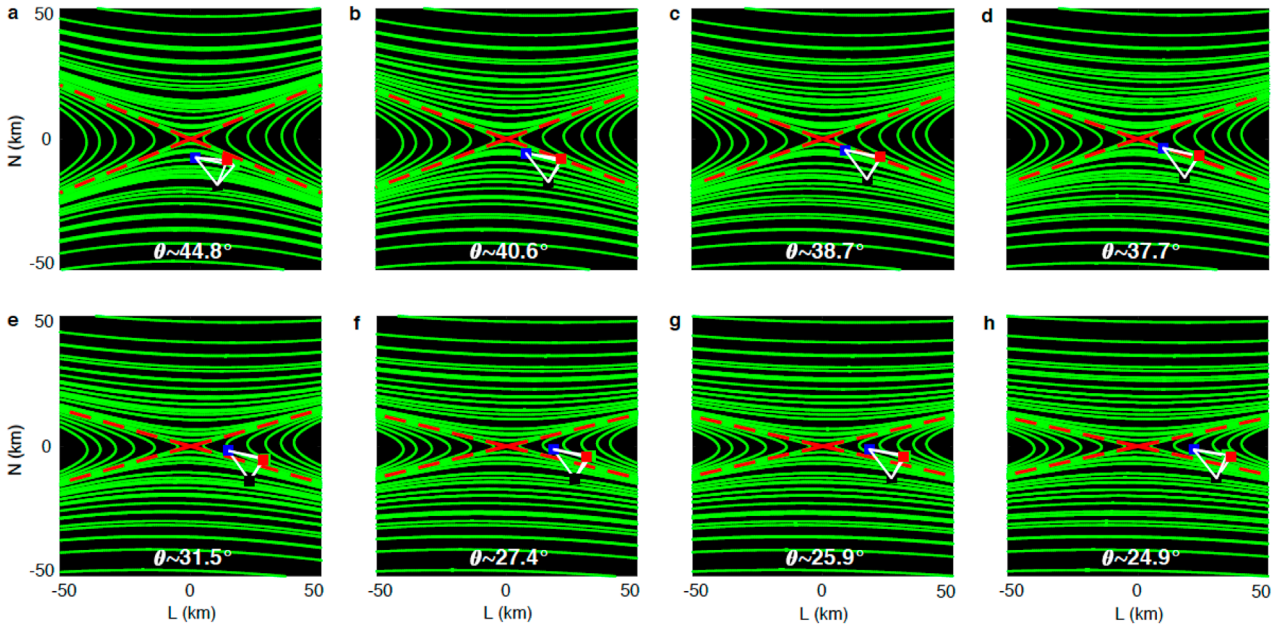

FIGURE 5
An example showing the application of the FOTE method to resolve the open angle of separatrix-lines during an unsteady reconnection. The angles between the two separatrix lines are **(A)** θ = 44°.8, **(B)** θ = 40°.6, **(C)** θ = 38°.7, **(D)** θ = 37°.7, **(E)** θ = 31°.5, **(F)** θ = 27°.4, **(G)** θ = 25°.9, **(H)** θ = 24°.9 (after Wang et al., 2020).

(2004a), Dunlop and Balogh (2005). The left panel shows that J orientations are predominantly in the MP plane during a number of in/out crossings resulting from magnetopause motion (average speed ~25 km/s; with average thicknesses ~1,200 km), while the right panel shows a thin MPBL with high current density. Typically, the Earth's magnetopause thickness varies from 100s of km (a few ion gyro radii) to 1,000s of km (Berchem and Russell, 1982; Paschmann et al., 2005; Panov et al., 2008), while corresponding current densities vary from 10 to 200 nA/m^2. In Figure 7A, the signatures outside the main MP crossing period are magnetosheath FTEs, where the current is along the mean reconnected flux tube direction (also studied by Pu et al., 2005).

Table 1 gives a summary of typical current density values in the Earth's environment, based on estimates of large-scale morphology and transient structure.

Figure 7 also illustrates that the combination of the curlometer and discontinuity analysis (which can obtain boundary orientation and motion (see Dunlop and Woodward, 1998; Dunlop et al., 2002; Haaland et al., 2004a) can confirm the thickness of the current layer and the alignment of J in the local MP plane. Broad scaling of |J| (10–50 nAm^{-2}) depending on a range of thicknesses, ΔD, can be shown to be consistent with the effective planar current $(\Delta B/\Delta D)/\mu_0$. The Cluster results tend to underestimate current for higher J and thicker boundary layers (compared to the separation). Indeed, the existence of small-scale sub-layers within the MPBL, having high intensity currents, were not often resolved by Cluster, but were seen by MMS (Dunlop et al., 2021a). The MVAJ method, referred to in the right panel of Figure 7 [see also Xiao et al. (2004), who apply the method to FTE orientations] better ties the orientation of the current sheet to J (minimum variance of J obtains the orientation of a near 1D current sheet, since div J = 0, when μ0J = curl B). The velocity of the current sheet can also be obtained (Haaland et al., 2004b), where different estimates of orientation all agree to within a few %.

A second key region demonstrating the capabilities of the curlometer became accessible after the launch of the multi-point measurements from Swarm at low-Earth orbit (LEO) altitudes. Although Swarm is a three-spacecraft mission and is not always in a close constellation, the method can be generalised by using nearby positions in time as indicated in Figure 1. This provides estimates even for only 2 or 3 closely separated spacecraft when either the dominant currents are field-aligned (FAC) or characteristic currents are locally static, [typical in this region of the high altitude ionosphere and thermosphere, e.g., Ritter and Lühr, 2006; Ritter et al., 2013; Dunlop et al., 2015a; Dunlop et al., 2015b; Dong et al., 2023, and references in Dunlop and Lühr (2020)]. Subtraction of the main, background field components prior to application of the method is essential At these low LEO altitudes (400–600 km), the main, background field must be subtracted to avoid the effect of zero current non-linear gradients [typically the IGRF or Chaos model (e.g., Olsen et al., 2014) are subtracted].

Typical convection times of ~10–15s apply in the case of the Swarm spacecraft separations of ~100–150 km at mid to high latitudes. Thus, the multi-spacecraft estimate depends on the FACs not being highly time dependent (e.g., ULF or Alfvén waves); but usually this is only relevant for small-scale currents, which can be easily identified by differences in field measured at the individual spacecraft. Thus, in addition to identifying smaller scale and time dependent structures, the extended methodology maps

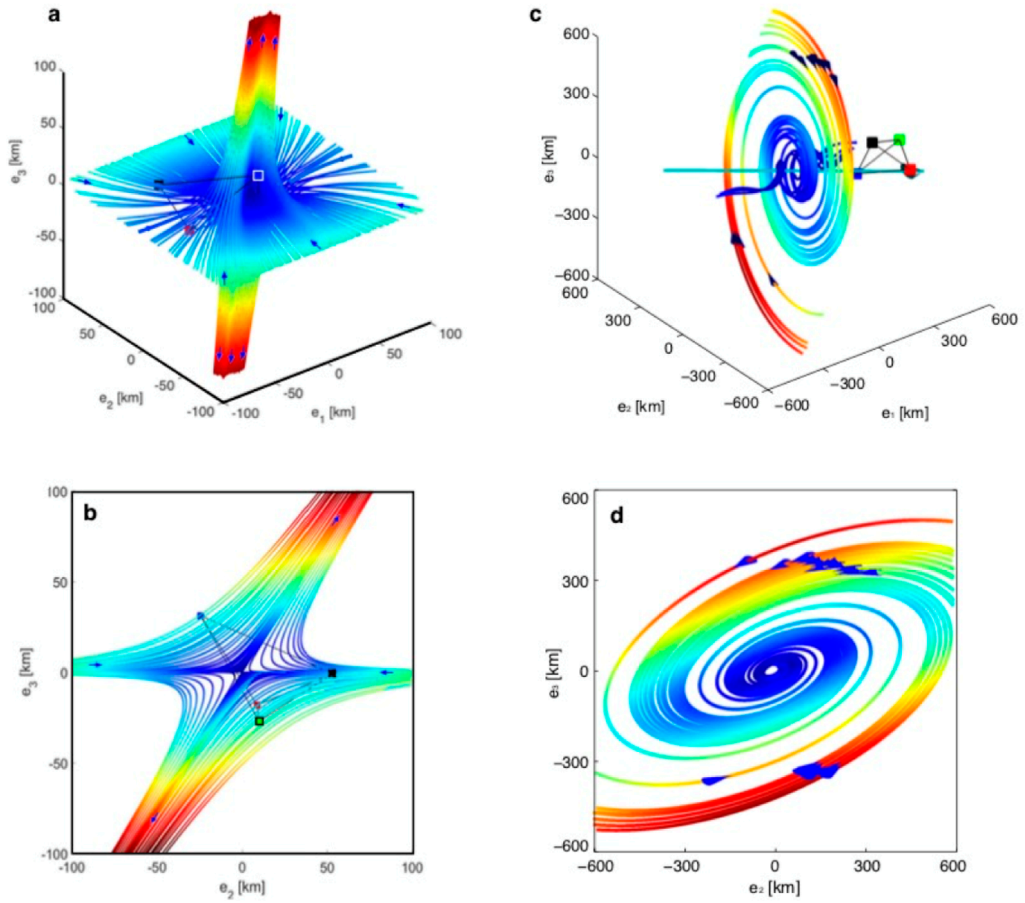

FIGURE 6
An example illustrating the application of the FOTE method to reconstruct the topology of a radial-type null and a spiral-type null (modified from Fu et al., 2017; Wang Z. et al., 2019). **(A)** Three-dimensional view of the radial-type null. **(B)** Two-dimensional view of the radial-type null. **(C)** Three-dimensional view of the spiral-type null. **(D)** Two-dimensional view of the spiral-type null.

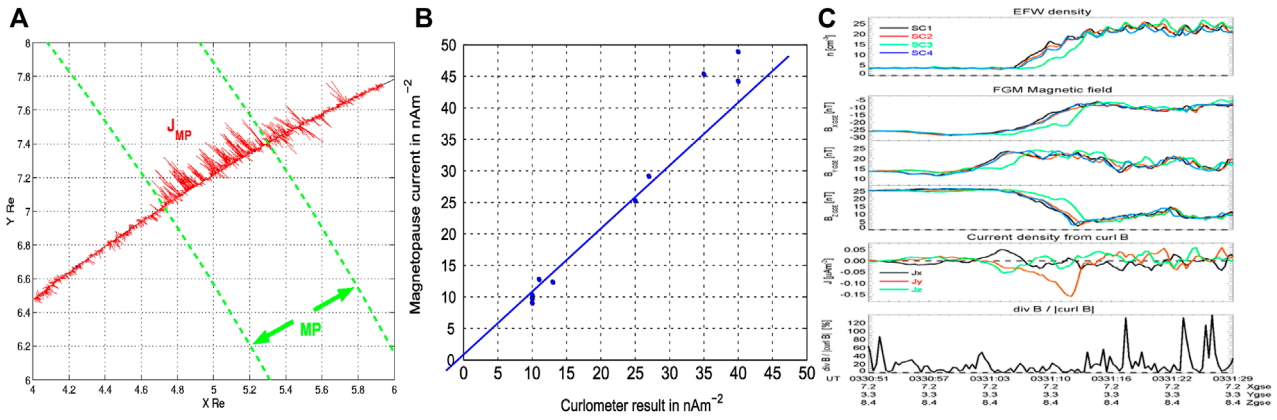

FIGURE 7
After Dunlop et al. (2021a): **(A)** Current density vectors for a period of MP oscillations on the 26 January 2001, showing alignment to the MP boundary **(B)** Comparison of the current density estimated from an equivalent Chapman-Ferraro sheet to the curlometer at the MP (from Dunlop and Balogh, 2005) **(C)** Plot of plasma density, magnetic field and current density (values of Q bottom panel), showing a thin magnetopause (on 2 March 2002), where the separations were ~100 km and estimated current densities reach 160 nAm^{-2}, extending over 200 km (Haaland et al., 2004b).

TABLE 1 Typical current density values (from Dunlop et al., 2021a).

Feature/Region	Typical values for J
Magnetopause currents	~10 nA m^{-2} (Dunlop and Eastwood, 2008), to 100 s nA m^{-2} (see, e.g., Panov et al., 2008)
Currents in flux transfer events	~1 nA m^{-2} (Dunlop and Eastwood, 2008) up to 10 nA m^{-2} (Pu et al., 2005)
Current at the cusp boundaries	~20 nA m^{-2} (Dunlop et al., 2002)
Field aligned currents (FAC)	~2 μA m^{-2} at 500 km altitude and ~20 nA m^{-2} at 2.5 RE altitude (Dunlop et al., 2005)
Magnetotail current sheet	up to ~30 nA m^{-2} (Runov et al., 2006)
Plasma sheet boundary layer	~10 nA m^{-2}, (Nakamura et al., 2004)
Ring current	9–27 nA m^{-2} at 4–4.5 RE, (Zhang et al., 2011)
Solar wind current sheet	~10 nA m^{-2} (Eastwood et al., 2002)

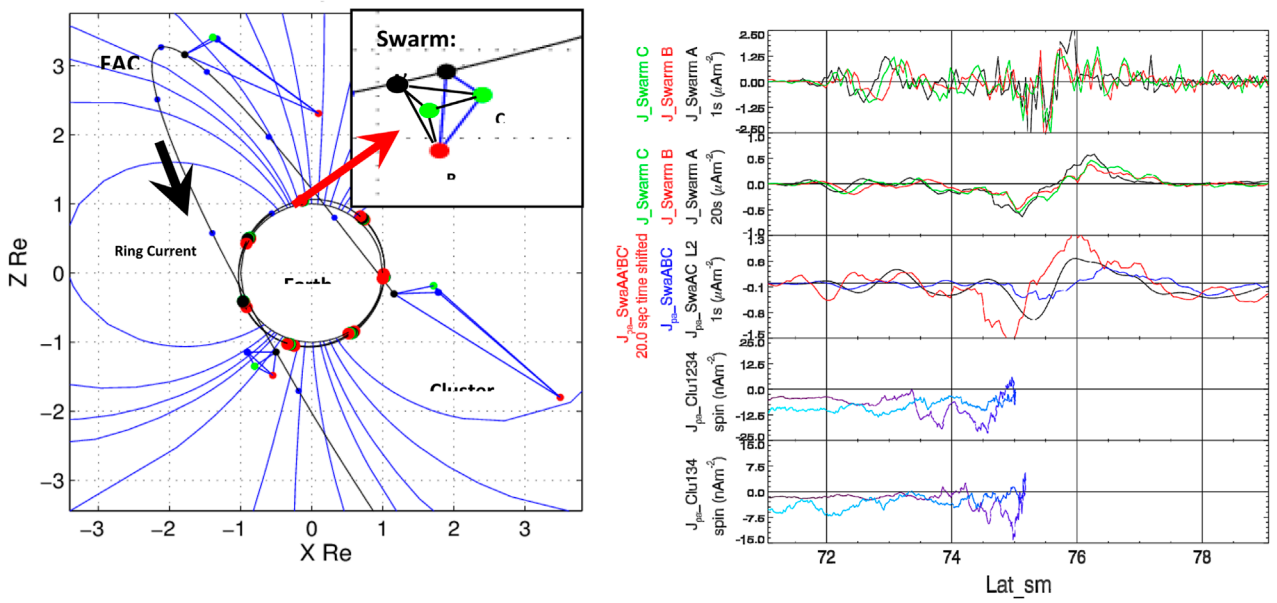

FIGURE 8
A Cluster and Swarm conjunction, taken from Dunlop et al. (2015a), projected into Z,X_{GSM} (left panel). Configurations of Cluster are enlarged by a factor of 3. Cluster moves from dusk (front) to dawn, moving from lower- to high-latitudes (marked FAC) near the R2 auroral boundary and back. The Swarm orbit lies close to Z,X_{GSM}, passing under the Cluster orbit and across the polar cap during the high-latitude Cluster positions. Thus, the magnetic footprints of Cluster cut across those of Swarm within minutes of the Swarm pass. The right-hand plots show Swarm and Cluster FAC estimates as a function of MLAT. The top two panels are unfiltered and 20s filtered, single spacecraft FACs (for Swarm A, B, C), while the middle panel shows different Swarm multi-spacecraft estimates (red line is the 4-point method; the blue line is the ABC planar configuration, and the smooth black line is the level 2 dual spacecraft estimate). Cluster FACs, estimated for the face perpendicular to the magnetic field, and the full curlometer are in the lower panels (where the dark blue trace is the initial crossing and the light blue trace corresponds to the times after the conjunction when Cluster moves back to lower latitudes at different local times (after Dunlop et al., 2021a).

out the morphology and dynamics of larger scale current systems, e.g., region 1, region 2 and NBZ FAC systems (see review in Mcpherron et al., 1973; Shiokawa et al., 1998; Cao et al., 2010).

Figure 1B shows the Swarm configuration, as considered in Dunlop et al. (2015a) for a close conjunction of Cluster and Swarm (as shown in Figure 8). A series of 2, 3 and 4 spacecraft estimates for the FACs can be made (in the context of the time shifted positions), while 4-spacecraft positions also give very low Q estimates (a few %). Changing the choice of the selected spacecraft positions can indicate how stable the estimates are (note that the effective barycentres of each set are slightly different). These comparative estimates are shown on the right-hand side of Figure 8, which also shows (top two panels) the filtered single spacecraft FAC estimates from *dB/dt* (Lühr et al., 2015). The 4-point estimates of the FAC profiles match those estimated from Cluster measurements most closely (with suitable scaling). Cluster moves to higher MLAT values

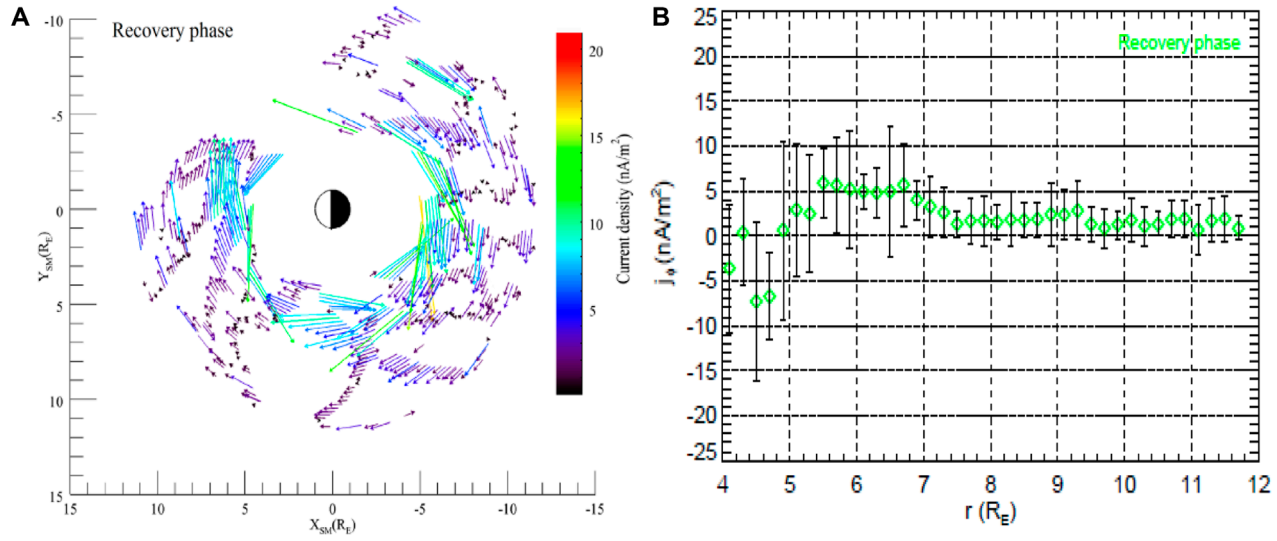

FIGURE 9
(A) Current densities projected into the ring plane are shown in a similar way (from THEMIS) for all storm activities during the recovery phase, showing the wider range of radial coverage achieved (for about 4–12 R_E) and an enhanced current near midnight LT for storm events. **(B)** Radial profile of the current density from THEMIS measurements (after Dunlop et al., 2021a).

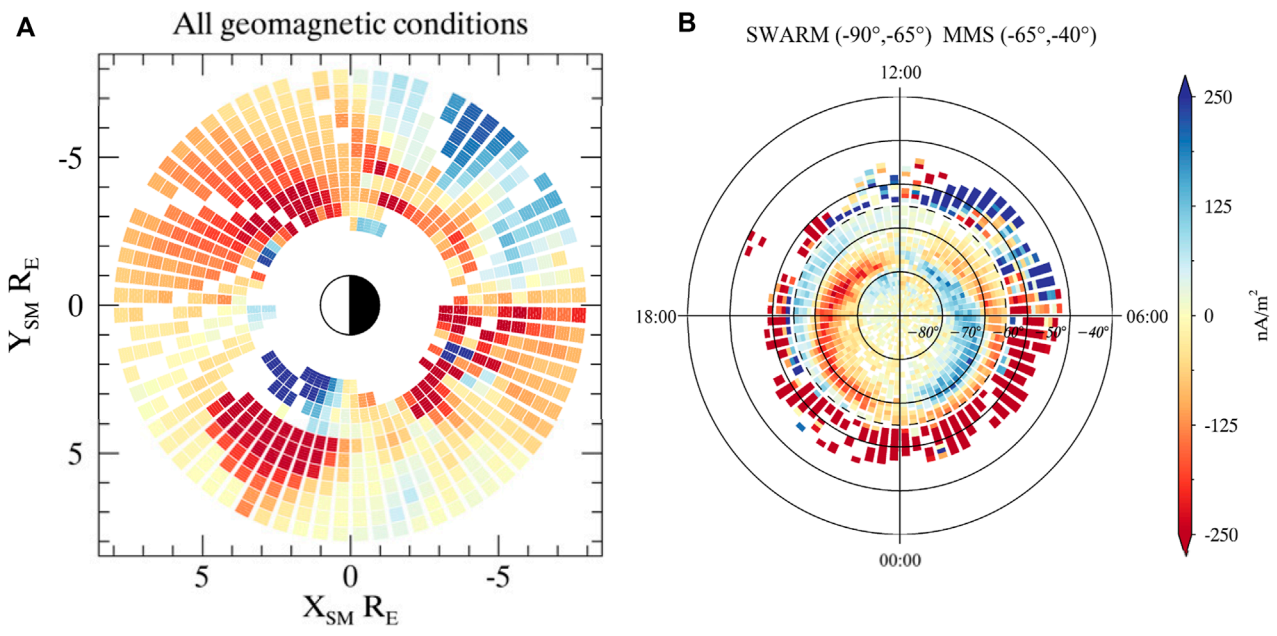

FIGURE 10
Plots of the morphology of current density in the ring current [**(A)**; from J_ϕ] and comparison of FACs from $J_{||}$, measured both adjacent to the RC and by Swarm in the ionosphere **(B)**, after Carter et al. (2024). Note that the $J_{||}$ current densities from MMS have been scaled in strength to the expected density at swarm altitudes. This is expected to be an overestimate, particularly for the sub-auroral regions.

and then back to lower MLAT in its traversal of the region but cross the local time of the Swarm orbit within minutes of the Swarm pass. The results imply that ~ 1–200 *km* Swarm currents (at LEO altitudes) can coherently map to Cluster.

The 4-point calculation can also identify any perpendicular components and estimates for this event appear to show possible, associated hall signatures consistent with wire model FACs (see Gjerloev and Hoffman, 2002; Ritter et al., 2004; Wang et al., 2006; Liang and Liu, 2007; Shore et al., 2013). Related methods dealing with FAC estimates have been cross-compared to assess key events by Trenchi et al. (2020) and a similar time-shifted Swarm configuration, tailored to the low latitude regions, has attempted to extract low latitude currents (Fillion et al., 2021).

A third key region, suitable for adaption of the curlometer is the Earth's ring current (RC). This was studied early with Cluster (Dandouras et al., 2018; Dunlop et al., 2018), and then using the

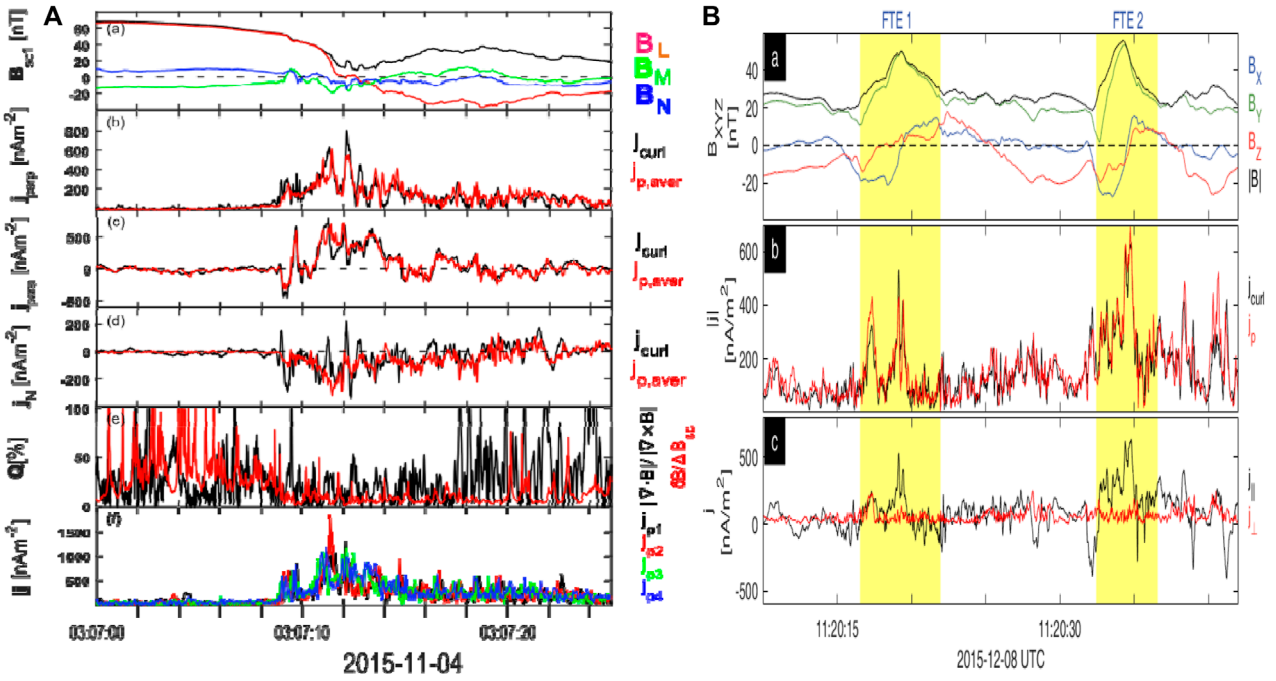

FIGURE 11
After Dunlop et al. (2021a): **(A)** A typical MP crossing for a thickness of ~350 km seen by MMS (after Dunlop et al., 2018), showing: (a) L, M, N coordinates of the magnetic field, (b) to (d) the perpendicular (Chapman-Ferraro), parallel (field-aligned) and normal components of both ***J*** from the curlometer estimate and the mean value of the 4-spacecraft ion moments, (e) the quality parameter Q compared to a crude (upper) estimate of the measurement errors from δB/ΔB, (f) the individual |***J***| from the plasma moments at each spacecraft. **(B)** Detailed current structures of two ion-scale FTEs: (a) magnetic field with bipolar signatures in the normal component (B_x) during each FTE interval; (b) A consistent current result from the curlometer and plasma moments, respectively, and (c) Parallel and perpendicular currents (after Dong et al., 2017).

3-spacecraft magnetospheric THEMIS spacecraft, as mentioned in Section 2.1. More recently MMS measurements have been used to estimate the ring current densities. There are contrasts between each: Cluster only accessed the mesoscale separations; the 3 THEMIS spacecraft limit the estimate to the normal current component, and MMS only has survey magnetic field data (with no thermal plasma) in the RC region. As first reported by Vallat et al. (2005), the Cluster polar orbit cuts north to south through the ring plane, allowing all local times to be scanned over the mission (Zhang et al., 2011) for a narrow range of radial distance (~4–4.5 R_E). Typically, the azimuthal component, J_ϕ, can be made, where the IGRF model is subtracted to reduce the effect of non-linear dipole gradients (mentioned in Section 2.1). Full azimuthal scans can highlight local time asymmetry in the RC and a possible relation to asymmetries at the MP has been suggested by Haaland and Gjerloev (2013).

As shown on the left-hand side of Figure 1, the three magnetospheric THEMIS spacecraft I near equatorial orbits also provide a wide MLT coverage (Yang et al., 2016), but for a range of radial distances, as shown in the left panel of Figure 9, so that L-shell profile can be revealed together with the Westward-Eastward current boundary on the inner edge of the RC, as shown in the right panel of Figure 9.

MMS also samples the ring current in a near equatorial orbit, providing a comparative RC estimate covering the same region as THEMIS on small separation scales. Thus, MMS can better resolve the trends seen in both the radial and azimuthal morphology, and also can identify small scale intense currents, which are not resolved by Cluster or THEMIS. The recent studies using MMS data (Tan et al., 2023), mentioned in Section 2.1 show both large and small-scale structures can be present, extending the earlier studies with Cluster and THEMIS. The morphology of the RC (left hand side of Figure 10) is broadly consistent with previous *in situ* studies with strong dawn/dusk and noon midnight asymmetry, but shows more detailed structure, with Tan et al. (2023) reporting a layered structure in latitude. A partial RC (or banana current), with an inner eastward current (blue) is most clear in the noon to dusk quadrant. There is no evidence of enhancement on the dusk-side during geomagnetically active periods.

Comparison of the Swarm low-altitude, dual-satellite FAC data with mapped MMS FAC signatures measured adjacent to the RC shows that RC behaviour and R2 FACs can be investigated directly (see right hand side of Figure 10) and show consistent patterns. The statistical coverage has some overlap in the location of Swarm FACs and the mapped locations of parallel currents measured adjacent to the RC (between 60 and 70 deg). In the auroral zone (particularly inside 65 deg, shown as a dashed circle), there is a qualitative R1/R2 pattern.

4.2 Recent application to MMS configuration scales

The current density can be obtained from velocity and density moments of the 3D plasma distributions for all ion species and

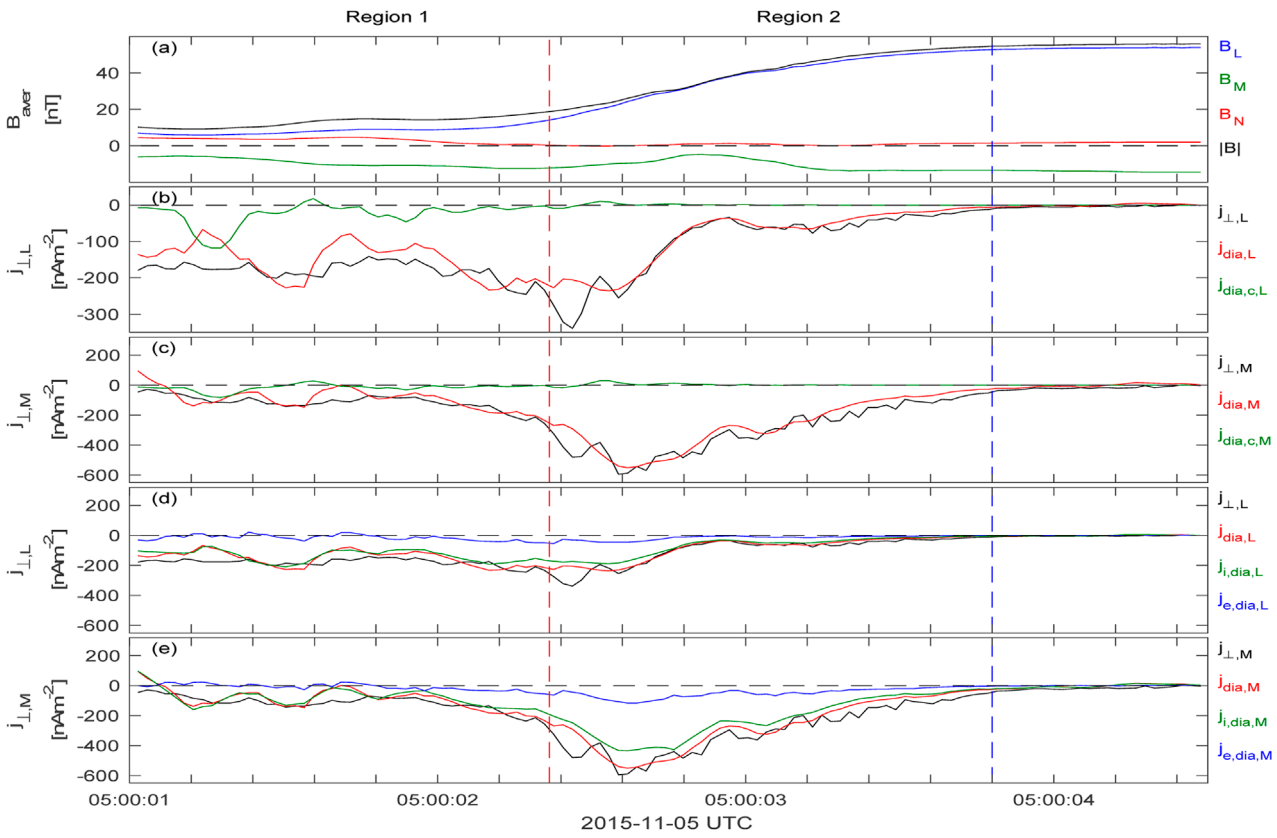

FIGURE 12
Sources of a thin magnetopause current sheet calculated by MMS data. **(A)** Four spacecraft average magnetic field; **(B, C)** perpendicular current from four spacecraft plasma moments $j_{\perp}$ (black), diamagnetic drift current j_{dia} (red), and curvature drift current j_{dia}, c (green); **(D, E)** perpendicular current $j_{\perp}$ (black), diamagnetic drift current jdia (red), and ion/electron diamagnetic drift current $j_{i,\,dia}$ (green)/$j_{e,\,dia}$ (blue). The Figure is adapted from Dong et al. (2018).

electrons. Cluster, for example, was limited to low cadence (since the full distribution is taken over a spacecraft spin period) and typically particle distributions are measured over a limited energy range [the use of particle moments previously can be found in Henderson et al. (2008), Petrukovich et al. (2015), and indeed (Yao et al., 2014), who also used pressure gradients to estimate the perpendicular current density]. The MMS mission can measure plasma distributions at high-time resolution (primarily in the outer magnetosphere). The MMS constellation is generally much smaller size than the prevailing ion structure, while the Cluster configuration was usually of order or greater than the MPBL, for example. In many regions of the magnetosphere there are intense small-scale currents which are missed on the separation scales of Cluster (100 s *km*) so typically the curlometer tends to underestimate the current density. On MMS separation scales, however, the ion-scale structures can be well resolved. A number of studies have used MMS plasma moments to estimate the currents (e.g., Lavraud et al., 2016; Phan et al., 2016) and comparing these estimates to the curlometer can reveal details of sub-structure; smaller scale current layers, and details of the current carriers. Moreover, Cluster and MMS conjunctions (for example, at different locations on the MP) provide the opportunity to compare across multiple spatial scales. Below we briefly show two aspects of this analysis [a more complete treatment d given in Dunlop et al. (2021a)].

4.2.1 Sub-structure in the MP and FTEs

The left-hand side of Figure 11 shows a typical MMS magnetopause crossing where the curlometer current densities are plotted with the current density estimated from the plasma moments $[(\boldsymbol{J} = \sum \boldsymbol{q n_s V_s} \sim \boldsymbol{q n}(\boldsymbol{V_i} - \boldsymbol{V_e})]$, which can be estimated at each spacecraft position. The plasma currents closely follow the curlometer when averaged over the four spacecraft positions. The normal component (panel d) shows the most significant differences between the plasma currents and the curlometer. Panel (e) shows that for currents below ~50 nAm^{-2} both the measurement errors and Q are significant. Despite the close curlometer agreement with the spatially averaged plasma current (i.e., the mean current over the tetrahedron), the estimates at each spacecraft (bottom panel) vary significantly between each position. This might suggest small scale (filamentary) structure within the magnetopause layer, where the dominant current carriers are measured by the plasma moments (this would be consistent with the intense, narrow bursts of current seen in the curlometer profiles), and appears to be typical of the magnetopause layer (Dong et al., 2017). This substructure was not well resolved by Cluster (except for the smallest separation scales) and the Cluster array tends to miss these filamentary currents.

Many recent MMS studies have also focused on the ion-scale structure of FTEs (e.g., Eastwood et al., 2016; Zhao et al., 2016;

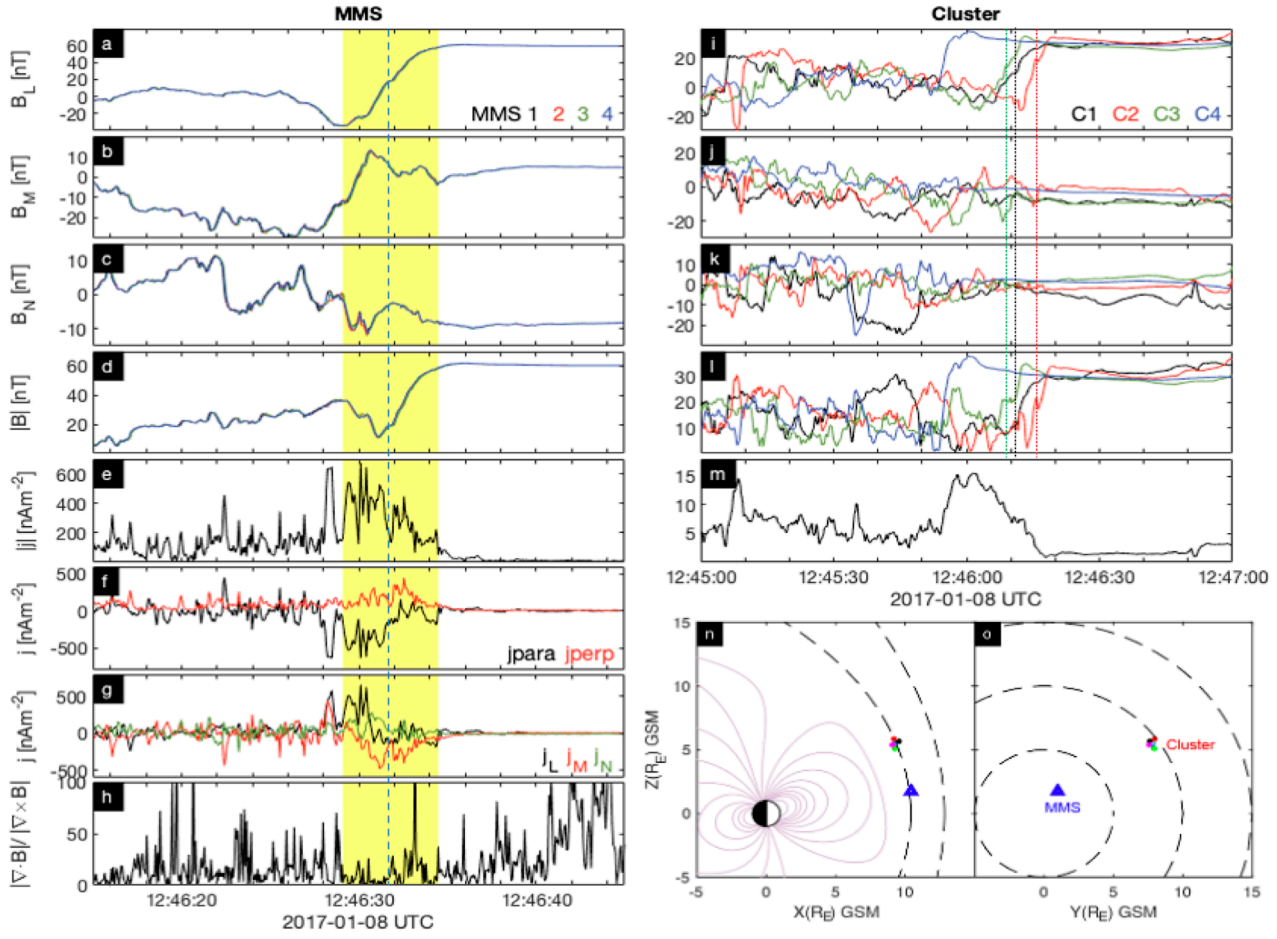

FIGURE 13
Magnetic field and current observed by a simultaneous MMS (left) and Cluster (right) magnetopause crossing (after Dunlop et al., 2021a). **(A–D, I–L)** Vector magnetic field in GSM coordinates. **(E, M)** Electric current from curlometer method. **(F)** MMS current in parallel and perpendicular direction, respectively. **(G)** MMS current in local boundary normal coordinate. **(N-O)** Magnetopause crossings locations of MMS ([10.4, 1.0, 1.8] R_E) and Cluster ([9.6, 7.6, 5.7] R_E) at XZ and YZ plane, respectively (safter Dunlop et al., 2021a).

Dong et al., 2017; Teh et al., 2017; Alm et al., 2018; Hwang et al., 2018; Dong et al., 2020). As first reported by Eastwood et al. (2016), agreement between the curlometer and plasma moments can be shown for current density in ion-scale FTEs, where filamentary currents were found and the main current carriers were electrons. The right-hand side of Figure 11 shows two ion-scale FTEs and their detailed current structures (Dong et al., 2017). The currents are highly inhomogeneous and mainly located in either the centre of the flux rope or on the leading edge [this was also true in the Roux et al. (2015) study of a large-scale FTE]. Central bifurcated features in the flux ropes were also present, while as a result of force-free structures, the parallel currents dominate.

4.2.2 Carriers and sources of magnetopause current

Figure 12 shows a thin MP current layer (~100 km) event encountered by MMS, which was studied by Dong et al. (2018). There is a comparable perpendicular current from the contributions of the ions and electrons in the boundary layer, but the parallel current appears to be dominated by the electron carriers. For the perpendicular currents, the diamagnetic current term ($\boldsymbol{J_{dia}} = \frac{B\times\nabla p_\perp}{B^2}$) and the directly measured $J_\perp$ shows good agreement (red line in Figures 12B, C) while the curvature current $\boldsymbol{J_{dia,c}} = -\frac{p_\parallel - p_\perp}{B^2 R_c}\boldsymbol{B}\times\boldsymbol{n}$ can be neglected (green line in Figures 12B, C). When the diamagnetic current is separated into ion and electron components, the perpendicular current is dominated by the ion diamagnetic current ($J_{i,dia}$: 85%, $J_{e,dia}$: 15%, Figures 12D, E). The ions and electrons ultimately carry comparable current through the redistribution of the electric field. The electron current deviates at a narrow front layer in region 2 which suggests non-MHD behaviour (beyond Chapman-Ferraro).

Note that the matched plasma and magnetic field measurements from MMS mean that the flow vorticity can be obtained from the curlometer estimates (Dunlop et al., 2002), providing linear estimates for velocity, in addition. Electron vorticities related with electron currents have been studied in the turbulent magnetosheath (Phan et al., 2016; Chasapis et al., 2018), and coherent Alfvén vortices in the same region (Wang T. et al., 2019) can be inferred from alignment of parallel current density and ion vorticity.

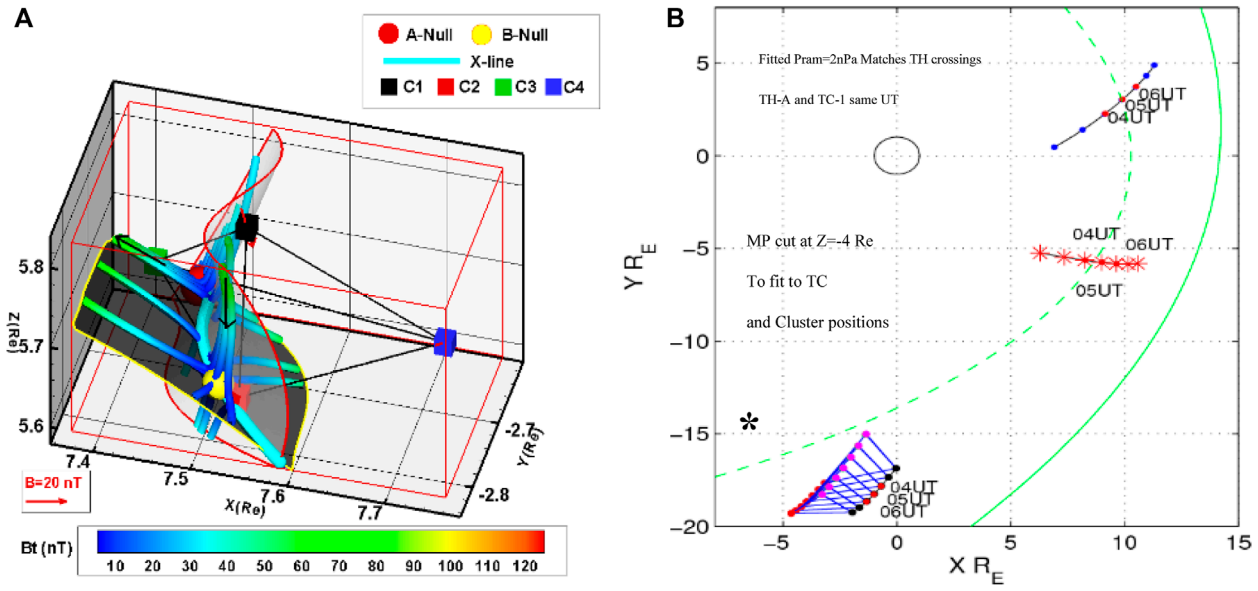

FIGURE 14
(A) Shows the reconstruction of an X-line geometry, where Cluster, located at high latitudes, repeatedly sampled magnetic nulls within the ion diffusion region, while Doublestar also sampled active reconnection signatures (FTEs) at low latitudes (after Dunlop et al., 2009). **(B)** A conjunction of the 5-THEMIS, 4-Cluster and 1-DSP spacecraft, covering a wide range of local time across the MP (after Dunlop et al., 2011) during periods of multiple, active reconnection sites, where all spacecraft are located at different positions along an extended, tilted (S-shaped) merging line.

4.2.3 Simultaneous MMS and cluster magnetopause crossings

A simultaneous MMS and Cluster crossing of the magnetopause (MPBL) at two different locations is shown in Figure 13, where MMS is located near the subsolar region and Cluster is located on the high latitude post-noon region (Figures 13N, O) and MMS crosses into the magnetosphere ~20 s later than Cluster. The MMS spacecraft are ~8 km apart, which is much smaller than the estimated current layer of ~440 km, while the Cluster spacecraft are ~3,500 km apart, which is large compared to the current layer at their location of ~1,400 km. Thus, the small-scale current structure can be resolved by MMS, while the overall MP current is underestimated by Cluster. In fact, the average MMS current (shaded region, Figure 13E) is ~220 nA/m^{-2}; one order of magnitude larger than estimated at Cluster (Figure 13M), although the simple 1-D (Chapman-Ferraro) current sheet estimated from the change in B and the thickness only differs by a factor of 2-3.

The parallel current measured by MMS (j_{para}) is dominant in the magnetosheath boundary layer, where magnetic field component B_L contra-rotates to a negative value (Figures 13A, F). This B_L feature is also observed by Cluster (Figure 13I), suggesting a similar current structure at both MMS and Cluster locations. The main MMS current sheet has a bifurcated structure, divided by a small current region, noted by the vertical dashed line. This small region corresponds to a flat B_L structure (Figure 13A), which is similar to that seen at Cluster 1, 2 and 3 (vertical dashed line, Figure 13I). This suggests the bifurcated current structure extends to the region of Cluster, but is not observed by Cluster 4 ~15 s beforehand, implying it is also highly dynamic.

Sampling the MPBL at two locations during specific IMF conditions has shown similar overall form for the magnetic field, suggesting that the MP can have similar current structure across a wide region. In another simultaneous event, however, studied by Escoubet et al. (2020) during a high-speed jet in the magnetosheath, the magnetopause current structures at Cluster and MMS are totally different. Similar current structures across a wide region may therefore only remain during relatively stable solar wind conditions.

5 Conclusion

The multi-spacecraft estimates of current density and spatial gradients from Cluster, and the later adaptions to the circumstances of the Swarm and MMS missions, have provided key information on large and small magnetospheric current systems and related transient structures, resolving 3-D currents for a range of conditions in widely different geospace regions. The curlometer in particular, has proved to be reliable and robust. The applicability of the method is limited by certain constraints, particularly those for relatively small structures compared to the spacecraft separation distances. These constraints depend on the form of the spacecraft configuration and the presence of magnetic contributions from other (non-current) sources. Particle moments, give direct, complementary current density estimates, which can be also used to add constraints in generalised methods computing magnetic gradients beyond linear order (Shen et al., 2021a; Shen et al., 2021c).

New constellation missions can make use of further adaptations of this multi-spacecraft methodology within the framework of extended arrays of more than four satellites, particularly when distributed across distinct spatial scales, where the comparative

results with MMS, Cluster and THEMIS, as illustrated here, can be re-visited. Figure 14 illustrates two early examples, where close conjunctions of Cluster, Doublestar and THEMIS were interpreted in the context of both local magnetopause structure and the larger scale surrounding phenomena, which provided evidence of the operation of multiple X-lines (see also the discussion in Section 4.2). The adaption of the various quality indicators have been considered, for example, to the new, proposed constellation missions, such as Plasma Observatory (Retinò et al., 2022) and Helioswarm (Klein et al., 2023). As discussed here, there is a balance between the use of either the Q divergence condition or the configuration shape (E and P), depending on the overall comparative spatial scale of the differential measurements. Where fast plasma measurements are available to produce high time resolution moments (n, V, T), then this information can help better resolve the spatial gradients on multiple spatial scales. Finally, we note here that the low frequency spectral response in the measurements (reflecting the time stationarity over the spacecraft arrays) will be an important consideration for applications to configurations of spacecraft which sample distinct spatial scales.

Plain text

This article is an account of analysis methods relating to spatial gradients obtained from the differential measurements taken by formations of multiple spacecraft. It focusses on the so named curlometer method, which uses four positions in space to estimate electric current density from the magnetic field. Originally, these measurements were from the set of four ESA Cluster II spacecraft. The curlometer produced many results throughout the magnetosphere, while more recently it has been applied to data from other missions of multiple spacecraft (the NASA MMS and THEMIS missions and the ESA Swarm Earth explorer mission). Although there are certain caviats on its application, the technique has proved to be rugged and stable. Other techniques, such as those estimating magnetic field geometry and gradients, have incorporated the curlometer and the application if these is also covered.

- Robust multi-spacecraft analysis method relating to spatial gradients.
- Estimates of the vector, *in situ*, electric current density directly.
- Wide application throughout the magnetosphere from magnetic field measurements.

Author contributions

MD: Conceptualization, Data curation, Funding acquisition, Methodology, Writing–original draft, Writing–review and editing. H-SF: Conceptualization, Investigation, Methodology, Writing–original draft. CS: Investigation, Methodology, Writing–original draft. XT: Data curation, Investigation, Methodology, Software, Writing–review and editing. X-CD: Conceptualization, Investigation, Methodology, Writing–review and editing. Y-YY: Conceptualization, Methodology, Writing–review and editing. PR: Conceptualization, Methodology, Writing–review and editing. PE: Data curation, Validation, Writing–review and editing.

Funding

The author(s) declare that financial support was received for the research, authorship, and/or publication of this article. This work is supported by the NSFC grants 42350710793, 41821003, 42174208; by NERC grants NE/P016863/1 and NE/W003309/1 and by STFC in-house research grant ST/M001083/1.

Acknowledgments

The Swarm satellite data used in this study are available from ESA at http://swarm-diss.eo.esa.int/. For MMS data visit https://lasp.colorado.edu/mms/sdc/public/. Cluster data can be found at http://www.cosmos.esa.int/web/csa/.

Conflict of interest

The authors declare that the research was conducted in the absence of any commercial or financial relationships that could be construed as a potential conflict of interest.

Publisher's note

References

Alm, L., Farrugia, C. J., Paulson, K. W., Argall, M. R., Torbert, R. B., Burch, J. L., et al. (2018). Differing properties of two ion-scale magnetopause flux ropes. *J. Geophys. Res. Space Phys.* 123, 114–131. doi:10.1002/2017JA024525

Angelopoulos, V. (2008). The THEMIS mission. *Space Sci. Rev.* 141, 5–34. doi:10.1007/s11214-008-9336-1

Angelopoulos, V. (2009). "The THEMIS mission," in *The THEMIS mission*. Editors J. L. Burch, and V. Angelopoulos (New York, NY: Springer), 5–34. doi:10.1007/978-0-387-89820-9_2

Berchem, J., and Russell, C. T. (1982). The thickness of the magnetopause current layer: ISEE 1 and 2 observations. *J. Geophys. Res. Space Phys.* 87, 2108–2114. doi:10.1029/JA087iA04p02108

Bittencourt, J. A. (2004). *Fundamentals of plasma physics*. New York, NY: Springer. doi:10.1007/978-1-4757-4030-1

Burch, J. L., Moore, T. E., Torbert, R. B., and Giles, B. L. (2016). Magnetospheric multiscale overview and science objectives. *Space Sci. Rev.* 199, 5–21. doi:10.1007/s11214-015-0164-9

Cao, J.-B., Yan, C., Dunlop, M., Reme, H., Dandouras, I., Zhang, T., et al. (2010). Geomagnetic signatures of current wedge produced by fast flows in a plasma sheet. *J. Geophys. Res. Space Phys.* 115. doi:10.1029/2009JA014891

Carter, J. A., Dunlop, M., Forsyth, C., Oksavik, K., Donovon, E., Kavanagh, A., et al. (2024). Ground-based and additional science support for SMILE. *Earth Planet. Phys.* 8, 275–298. doi:10.26464/epp2023055

Chanteur, G. (1998). "Spatial interpolation for four spacecraft: theory," in *Analysis methods for multi-spacecraft data*. Editors G. Paschmann, and P. W. Daly (Noordwijk, Netherlands: ESA Publications Division), 349–370.

Chanteur, G., and Harvey, C. C. (1998). "Spatial interpolation for four spacecraft: application to magnetic gradients," in *Analysis methods for multi-spacecraft data*. Editors G. Paschmann, and P. W. Daly (Noordwijk, Netherlands: ESA Publications Division), 371–394.

Chasapis, A., Yang, Y., Matthaeus, W. H., Parashar, T. N., Haggerty, C. C., Burch, J. L., et al. (2018). Energy conversion and collisionless plasma dissipation channels in the turbulent magnetosheath observed by the magnetospheric multiscale mission. *Astrophysical J.* 862, 32. doi:10.3847/1538-4357/aac775

Chen, X. H., Fu, H. S., Liu, C. M., Cao, D., Wang, Z., Dunlop, M. W., et al. (2018). Magnetic nulls in the reconnection driven by turbulence. *Astrophysical J.* 852, 17. doi:10.3847/1538-4357/aa9991

Chen, Z. Z., Fu, H. S., Wang, Z., Liu, C. M., and Xu, Y. (2019). Evidence of magnetic nulls in the reconnection at bow shock. *Geophys. Res. Lett.* 46, 10209–10218. doi:10.1029/2019GL084360

Dai, L., Wang, C., Cai, Z., Gonzalez, W., Hesse, M., Escoubet, P., et al. (2020). AME: a cross-scale constellation of CubeSats to explore magnetic reconnection in the solar-terrestrial relation. *Front. Phys.* 8, 89. doi:10.3389/fphy.2020.00089

Dandouras, I., Rochel-Grimald, S., Vallat, C., and Dunlop, M. W. (2018). "Terrestrial ring current: a review of cluster results based on the curlometer technique," in *Electric currents in geospace and beyond. American geophysical union*. Editors A. Keiling, O. Marghitu, and M. Wheatland (John Wiley and Sons), 115–126. doi:10.1002/9781119324522.ch7

De Keyser, J. (2008). Least-squares multi-spacecraft gradient calculation with automatic error estimation. *Ann. Geophys.* 26, 3295–3316. doi:10.5194/angeo-26-3295-2008

De Keyser, J., Darrouzet, F., Dunlop, M. W., and Décréau, P. M. E. (2007). Least-squares gradient calculation from multi-point observations of scalar and vector fields: methodology and applications with Cluster in the plasmasphere. *Ann. Geophys.* 25, 971–987. doi:10.5194/angeo-25-971-2007

Denton, R. E., Liu, Y.-H., Hasegawa, H., Torbert, R. B., Li, W., Fuselier, S., et al. (2022). Polynomial reconstruction of the magnetic field observed by multiple spacecraft with integrated velocity determination. *J. Geophys. Res.* 127. doi:10.1029/2022JA030512

Denton, R. E., Torbert, R. B., Hasegawa, H., Dors, I., Genestreti, K. J., Argall, M. R., et al. (2020). Polynomial reconstruction of the reconnection magnetic field observed by multiple spacecraft. *J. Gephys. Res.* 125. doi:10.1029/2019JA027481

Dong, X. C., Dunlop, M. W., Trattner, K. J., Phan, T. D., Fu, H. S., Cao, J. B., et al. (2017). Structure and evolution of flux transfer events near dayside magnetic reconnection dissipation region: MMS observations. *Geophys. Res. Lett.* 44, 5951–5959. doi:10.1002/2017gl073411

Dong, X. C., Dunlop, M. W., Wang, T. Y., Cao, J. B., Trattner, K. J., Bamford, R., et al. (2018). Carriers and sources of magnetopause current: MMS case study. *J. Geophys. Res. Space Phys.* 123, 5464–5475. doi:10.1029/2018ja025292

Dong, X. C., Dunlop, M. W., Wang, T. Y., Trattner, K. J., Russell, C. T., and Giles, B. (2020). MMS observation of secondary magnetic reconnection beside ion-scale flux rope at the magnetopause. *Geophys. Res. Lett.* 47. doi:10.1029/2020gl089075

Dong, X. C., Dunlop, M. W., Xiao, C., Wei, D., Wang, T. Y., and Zhao, J. S. (2023). Simultaneous mesoscale polar cusp field-aligned currents measured on mid- and low-altitude satellites. *Geophys. Res. Lett.* 50, e2022GL102460. doi:10.1029/2022GL102460

Dunlop, M. W., and Balogh, A. (2005). Magnetopause current as seen by Cluster. *Ann. Geophys.* 23, 901–907. doi:10.5194/angeo-23-901-2005

Dunlop, M. W., Balogh, A., Glassmeier, K. H., and Robert, P. (2002). Four-point Cluster application of magnetic field analysis tools: the Curlometer. *J. Geophys. Res. Space Phys.* 107. doi:10.1029/2001ja005088

Dunlop, M. W., Dong, X. C., Wang, T. Y., Eastwood, J. P., Robert, P., Haaland, S., et al. (2021a). Curlometer technique and applications. *J. Geophys. Res. Space Phys.* 126. doi:10.1029/2021ja029538

Dunlop, M. W., and Eastwood, J. P. (2008). "The curlometer and other gradient based methods," in *Multi-spacecraft analysis methods revisited*. Editors G. Paschmann, and P. W. Daly (Noordwijk, Netherlands: ESA Communications Keplerlaan), 17–26.

Dunlop, M. W., Haaland, S., Dong, X. C., Middleton, H. R., Escoubet, C. P., Yang, Y. Y., et al. (2018). "Multipoint analysis of electric currents in geospace using the curlometer technique," in *Electric currents in geospace and beyond. American geophysical union*. Editors A. Keiling, O. Marghitu, and M. Wheatland (John Wiley and Sons), 67–80. doi:10.1002/9781119324522.ch4

Dunlop, M. W., and Lühr, H. (2020). *Ionospheric multi-spacecraft analysis tools*. Springer. doi:10.1007/978-3-030-26732-2

Dunlop, M. W., Southwood, D. J., Glassmeier, K. H., and Neubauer, F. M. (1988). Analysis of multipoint magnetometer data. *Adv. Space Res.* 8, 273–277. doi:10.1016/0273-1177(88)90141-X

Dunlop, M. W., Taylor, M. G. G. T., Davies, J. A., Owen, C. J., Pu, Z., Laakso, H., et al. (2005). Coordinated cluster/double star observations of dayside reconnection signatures. *Ann. Geophys.* 23 (8), 2867–2875.

Dunlop, M. W., Wang, T., Dong, X., Haarland, S., Shi, Q., Fu, H., et al. (2021b). "Multispacecraft measurements in the magnetosphere," in *Magnetospheres in the solar system. American geophysical union*. Editors R. Maggiolo, N. André, H. Hasegawa, and D. T. Welling (John Wiley and Sons), 637–656. doi:10.1002/9781119815624.ch40

Dunlop, M. W., and Woodward, T. I. (1998). "Multi-spacecraft discontinuity analysis: orientation and motion," in *Analysis methods for multi-spacecraft data*. Editors G. Paschmann, and P. W. Daly (Noordwijk, Netherlands: ESA Publications Division), 271–306.

Dunlop, M. W., Yang, J. Y., Yang, Y. Y., Lühr, H., and Cao, J. B. (2020). "Multi-spacecraft current estimates at swarm," in *Ionospheric multi-spacecraft analysis tools*. Editors M. W. Dunlop, and H. Lühr (Springer), 83. doi:10.1007/978-3-030-26732-2_5

Dunlop, M. W., Yang, J. Y., Yang, Y. Y., Xiong, C., Lühr, H., Bogdanova, Y. V., et al. (2015a). Simultaneous field-aligned currents at Swarm and Cluster satellites. *Geophys. Res. Lett.* 42, 3683–3691. doi:10.1002/2015gl063738

Dunlop, M. W., Yang, Y. Y., Yang, J. Y., Lühr, H., Shen, C., Olsen, N., et al. (2015b). Multispacecraft current estimates at swarm. *J. Geophys. Res. Space Phys.* 120, 8307–8316. doi:10.1002/2015ja021707

Dunlop, M. W., Zhang, Q.-H., Bogdanova, Y. V., Lockwood, M., Pu, Z., Hasegawa, H., et al. (2011). Extended magnetic reconnection across the dayside magnetopause. *Phys. Rev. Lett.* 107, 025004. doi:10.1103/PhysRevLett.107.025004

Dunlop, M. W., Zhang, Q. H., Xiao, C. J., He, J. S., Pu, Z., Fear, R. C., et al. (2009). Reconnection at high latitudes: antiparallel merging. *Phys. Rev. Lett.* 102, 075005. doi:10.1103/PhysRevLett.102.075005

Eastwood, J. P., Balogh, A., Dunlop, M. W., and Smith, C. W. (2002). Cluster observations of the heliospheric current sheet and an associated magnetic flux rope and comparisons with ACE. *J. Geophys. Res. Space Phys.* 107 (SSH 9-1), 9. doi:10.1029/2001JA009158

Eastwood, J. P., Phan, T. D., Cassak, P. A., Gershman, D. J., Haggerty, C., Malakit, K., et al. (2016). Ion-scale secondary flux ropes generated by magnetopause reconnection as resolved by MMS. *Geophys. Res. Lett.* 43, 4716–4724. doi:10.1002/2016GL068747

Escoubet, C. P., Fehringer, M., and Goldstein, M. (2001). *Introduction*The cluster mission. *Ann. Geophys.* 19, 1197–1200. doi:10.5194/angeo-19-1197-2001

Escoubet, C. P., Hwang, K. J., Toledo-Redondo, S., Turc, L., Haaland, S. E., Aunai, N., et al. (2020). Cluster and MMS simultaneous observations of magnetosheath high speed jets and their impact on the magnetopause. *Front. Astronomy Space Sci.* 6, 78. doi:10.3389/fspas.2019.00078

Escoubet, C. P., Masson, A., Laakso, H., Goldstein, M. L., Dimbylow, T., Bogdanova, Y. V., et al. (2021). Cluster after 20 years of operations: science highlights and technical challenges. *J. Geophys. Res. Space Phys.* 126, e29474. doi:10.1029/2021JA029474

Escoubet, C. P., Schmidt, R., and Goldstein, M. L. (1997). Cluster - science and mission overview. *Space Sci. Rev.* 79, 11–32. doi:10.1023/A:1004923124586

Fillion, M., Hulot, G., Alken, P., Chulliat, A., and Vigneron, P. (2021). Multispacecraft current density estimates in the low- and mid-latitude F-region ionosphere using the swarm constellation. *J. Geophys. Res. Space Phys.* 126, e28872. doi:10.1029/2020JA028872

Forsyth, C., Lester, M., Cowley, S. W. H., Dandouras, I., Fazakerley, A. N., Fear, R. C., et al. (2008). Observed tail current systems associated with bursty bulk flows and auroral streamers during a period of multiple substorms. *Ann. Geophys.* 26, 167–184. doi:10.5194/angeo-26-167-2008

Forsyth, C., Lester, M., Fazakerley, A. N., Owen, C. J., and Walsh, A. P. (2011). On the effect of line current width and relative position on the multi-spacecraft curlometer technique. *Planet. Space Sci.* 59, 598–605. doi:10.1016/j.pss.2009.12.007

Friis-Christensen, E., Lühr, H., and Hulot, G. (2006). Swarm: a constellation to study the Earth's magnetic field. *Earth, Planets Space* 58, 351–358. doi:10.1186/BF03351933

Friis-Christensen, E., Lühr, H., Knudsen, D., and Haagmans, R. (2008). Swarm – an Earth observation mission investigating geospace. *Adv. Space Res.* 41, 210–216. doi:10.1016/j.asr.2006.10.008

Fu, H. S., Cao, J. B., Cao, D., Wang, Z., Vaivads, A., Khotyaintsev, Y. V., et al. (2019). Evidence of magnetic nulls in electron diffusion region. *Geophys. Res. Lett.* 46, 48–54. doi:10.1029/2018GL080449

Fu, H. S., Cao, J. B., Vaivads, A., Khotyaintsev, Y. V., Andre, M., Dunlop, M., et al. (2016). Identifying magnetic reconnection events using the FOTE method. *J. Geophys. Res. Space Phys.* 121, 1263–1272. doi:10.1002/2015JA021701

Fu, H. S., Vaivads, A., Khotyaintsev, Y. V., André, M., Cao, J. B., Olshevsky, V., et al. (2017). Intermittent energy dissipation by turbulent reconnection. *Geophys. Res. Lett.* 44, 37–43. doi:10.1002/2016GL071787

Fu, H. S., Vaivads, A., Khotyaintsev, Y. V., Olshevsky, V., André, M., Cao, J. B., et al. (2015). How to find magnetic nulls and reconstruct field topology with MMS data? *J. Geophys. Res. Space Phys.* 120, 3758–3782. doi:10.1002/2015ja021082

Fu, H. S., Wang, Z., Zong, Q., Chen, X. H., He, J. S., Vaivads, A., et al. (2020). "Methods for finding magnetic nulls and reconstructing field topology," in *Dayside magnetosphere interactions*. *American geophysical union*. Editors Q. Zong, P. Escoubet, D. Sibeck, G. Le, and H. Zhang (John Wiley and Sons), 153–172. doi:10.1002/9781119509592.ch9

Gjerloev, J. W., and Hoffman, R. A. (2002). Currents in auroral substorms. *J. Geophys. Res. Space Phys.* 107 (SMP 5-1), 5–13. doi:10.1029/2001JA000194

Grimald, S., Dandouras, I., Robert, P., and Lucek, E. (2012). Study of the applicability of the curlometer technique with the four Cluster spacecraft in regions close to Earth. *Ann. Geophys.* 30, 597–611. doi:10.5194/angeo-30-597-2012

Haaland, S., and Gjerloev, J. (2013). On the relation between asymmetries in the ring current and magnetopause current. *J. Geophys. Res. Space Phys.* 118, 7593–7604. doi:10.1002/2013ja019345

Haaland, S., Hasegawa, H., Paschmann, G., Sonnerup, B., and Dunlop, M. (2021). 20 Years of cluster observations: the magnetopause. *J. Geophys. Res. Space Phys.* 126, e2021JA029362. doi:10.1029/2021JA029362

Haaland, S., Sonnerup, B., Dunlop, M., Balogh, A., Georgescu, E., Hasegawa, H., et al. (2004a). Four-spacecraft determination of magnetopause orientation, motion and thickness: comparison with results from single-spacecraft methods. *Ann. Geophys.* 22, 1347–1365. doi:10.5194/angeo-22-1347-2004

Haaland, S., Sonnerup, B. U. Ö., Dunlop, M. W., Georgescu, E., Paschmann, G., Klecker, B., et al. (2004b). Orientation and motion of a discontinuity from Cluster curlometer capability: minimum variance of current density. *Geophys. Res. Lett.* 31. doi:10.1029/2004GL020001

Hamrin, M., Rönnmark, K., Börlin, N., Vedin, J., and Vaivads, A. (2008). GALS – gradient analysis by least squares. *Ann. Geophys.* 26, 3491–3499. doi:10.5194/angeo-26-3491-2008

Harvey, C. C. (1998). "Spatial gradients and the volumetric tensor," in *Analysis methods for multi-spacecraft data*. Editors G. Paschmann, and P. W. Daly (Noordwijk, Netherlands: ESA Publications Division), 307–322.

He, J. S., Tu, C. Y., Tian, H., Xiao, C. J., Wang, X. G., Pu, Z. Y., et al. (2008a). A magnetic null geometry reconstructed from Cluster spacecraft observations. *J. Geophys. Res. Space Phys.* 113. doi:10.1029/2007JA012609

He, J. S., Zong, Q. G., Deng, X. H., Tu, C. Y., Xiao, C. J., Wang, X. G., et al. (2008b). Electron trapping around a magnetic null. *Geophys. Res. Lett.* 35, L14104. doi:10.1029/2008GL034085

Henderson, P. D., Owen, C. J., Lahiff, A. D., Alexeev, I. V., Fazakerley, A. N., Yin, L., et al. (2008). The relationship between $\mathbf{j} \times \mathbf{B}$ and $\nabla \cdot \mathbf{P}_e$ in the magnetotail plasma sheet: cluster observations. *J. Geophys. Res. Space Phys.* 113. doi:10.1029/2007ja012697

Hwang, K. J., Sibeck, D. G., Burch, J. L., Choi, E., Fear, R. C., Lavraud, B., et al. (2018). Small-scale flux transfer events formed in the reconnection exhaust region between two X lines. *J. Geophys. Res. Space Phys.* 123, 8473–8488. doi:10.1029/2018JA025611

Klein, K. G., Spence, H., Alexandrova, O., Argall, M., Arzamasskiy, L., Bookbinder, J., et al. (2023). HelioSwarm: a multipoint, multiscale mission to characterize turbulence. *Space Sci. Rev.* 219, 74. doi:10.1007/s11214-023-01019-0

Lavraud, B., Zhang, Y. C., Vernisse, Y., Gershman, D. J., Dorelli, J., Cassak, P. A., et al. (2016). Currents and associated electron scattering and bouncing near the diffusion region at Earth's magnetopause. *Geophys. Res. Lett.* 43, 3042–3050. doi:10.1002/2016GL068359

Liang, J., and Liu, W. W. (2007). A MHD mechanism for the generation of the meridional current system during substorm expansion phase. *J. Geophys. Res. Space Phys.* 112. doi:10.1029/2007JA012303

Lühr, H., Park, J., Gjerloev, J. W., Rauberg, J., Michaelis, I., Merayo, J. M. G., et al. (2015). Field-aligned currents' scale analysis performed with the Swarm constellation. *Geophys. Res. Lett.* 42, 1–8. doi:10.1002/2014gl062453

Marchaudon, A., Cerisier, J. C., Dunlop, M. W., Pitout, F., Bosqued, J. M., and Fazakerley, A. N. (2009). Shape, size, velocity and field-aligned currents of dayside plasma injections: a multi-altitude study. *Ann. Geophys.* 27, 1251–1266. doi:10.5194/angeo-27-1251-2009

McPherron, R. L., Russell, C. T., and Aubry, M. P. (1973). Satellite studies of magnetospheric substorms on August 15, 1968: 9. Phenomenological model for substorms. *J. Geophys. Res.* 78, 3131–3149. doi:10.1029/JA078i016p03131

Middleton, H. R., and Masson, A. (2016). The Curlometer Technique: a beginner's guide. Available at: http://www.cosmos.esa.int/web/csa/multi-spacecraft (Accessed April 11, 2024).

Nakamura, R., Baumjohann, W., Fujimoto, M., Asano, Y., Runov, A., Owen, C. J., et al. (2008). Cluster observations of an ion-scale current sheet in the magnetotail under the presence of a guide field. *J. Geophys. Res. Space Phys.* 113. doi:10.1029/2007JA012760

Narita, Y., Nakamura, R., and Baumjohann, W. (2013). Cluster as current sheet surveyor in the magnetotail. *Ann. Geophys.* 31, 1605–1610. doi:10.5194/angeo-31-1605-2013

Olsen, N., Lühr, H., Finlay, C., Sabaka, T., Michaelis, I., Rauberg, J., et al. (2014). The CHAOS-4 geomagnetic field model. *Geophys. J. Int.* 197, 815–827. doi:10.1093/gji/ggu033

Panov, E. V., Büchner, J., Fränz, M., Korth, A., Savin, S. P., Fornaçon, K. H., et al. (2006). CLUSTER observation of collisionless transport at the magnetopause. *Geophys. Res. Lett.* 33. doi:10.1029/2006GL026556

Panov, E. V., Büchner, J., Fränz, M., Korth, A., Savin, S. P., Rème, H., et al. (2008). High-latitude Earth's magnetopause outside the cusp: cluster observations. *J. Geophys. Res. Space Phys.* 113. doi:10.1029/2006ja012123

Paschmann, G., and Daly, P. W. (1998). *Analysis methods for multi-spacecraft data*. Noordwijk, Netherlands: ESA Publications Division.

Paschmann, G., and Daly, P. W. (2008). *Multi-spacecraft analysis methods revisited*. Noordwijk, Netherlands: ESA Communications Keplerlaan.

Paschmann, G., Schwartz, S. J., Escoubet, C. P., and Haaland, S. (2005). *Outer magnetospheric boundaries: cluster results*. Springer/ISSI. doi:10.1007/1-4020-4582-4

Petrukovich, A., Artemyev, A., Vasko, I., Nakamura, R., and Zelenyi, L. (2015). Current sheets in the Earth magnetotail: plasma and magnetic field structure with cluster project observations. *Space Sci. Rev.* 188, 311–337. doi:10.1007/s11214-014-0126-7

Phan, T. D., Eastwood, J. P., Cassak, P. A., Øieroset, M., Gosling, J. T., Gershman, D. J., et al. (2016). MMS observations of electron-scale filamentary currents in the reconnection exhaust and near the X line. *Geophys. Res. Lett.* 43, 6060–6069. doi:10.1002/2016GL069212

Pitout, F., and Bogdanova, Y. V. (2021). The polar cusp seen by cluster. *J. Geophys. Res. Space Phys.* 126, e2021JA029582. doi:10.1029/2021JA029582

Pu, Z. Y., Zong, Q. G., Fritz, T. A., Xiao, C. J., Huang, Z. Y., Fu, S. Y., et al. (2005). Multiple flux rope events at the high-latitude magnetopause: cluster/rapid observation on 26 january, 2001. *Surv. Geophys.* 26, 193–214. doi:10.1007/s10712-005-1878-0

Retinò, A., Khotyaintsev, Y., Le Contel, O., Marcucci, M. F., Plaschke, F., Vaivads, A., et al. (2022). Particle energization in space plasmas: towards a multi-point, multi-scale plasma observatory. *Exp. Astron.* 54, 427–471. doi:10.1007/s10686-021-09797-7

Ritter, P., and Lühr, H. (2006). Curl-B technique applied to Swarm constellation for determining field-aligned currents. *Earth, Planets Space* 58, 463–476. doi:10.1186/BF03351942

Ritter, P., Lühr, H., and Rauberg, J. (2013). Determining field-aligned currents with the Swarm constellation mission. *Earth, Planets Space* 65, 1285–1294. doi:10.5047/eps.2013.09.006

Ritter, P., Lühr, H., Viljanen, A., Amm, O., Pulkkinen, A., and Sillanpää, I. (2004). Ionospheric currents estimated simultaneously from CHAMP satelliteand IMAGE ground-based magnetic field measurements: a statisticalstudy at auroral latitudes. *Ann. Geophys.* 22, 417–430. doi:10.5194/angeo-22-417-2004

Robert, P., and Dunlop, M. W. (2022). Use of twenty years CLUSTER/FGM data to observe the mean behavior of the magnetic field and current density of Earth's magnetosphere. *J. Geophys. Res. Space Phys.* 127. doi:10.1029/2021ja029837

Robert, P., Dunlop, M. W., Roux, A., and Chanteur, G. (1998a). "Accuracy of current density determination," in *Analysis methods for multi-spacecraft data*. Editors G. Paschmann, and P. W. Daly (Noordwijk, Netherlands: ESA Publications Division), 395–418.

Robert, P., Roux, A., Harvey, C. C., Dunlop, M. W., Daly, P. W., and Glassmeier, K.-H. (1998b). "Tetrahedron geometric factors," in *Analysis methods for multi-spacecraft data*. Editors G. Paschmann, and P. W. Daly (Noordwijk, Netherlands: ESA Publications Division), 323–348.

Rong, Z. J., Wan, W. X., Shen, C., Li, X., Dunlop, M. W., Petrukovich, A. A., et al. (2011). Statistical survey on the magnetic structure in magnetotail current sheets. *J. Geophys. Res. Space Phys.* 116. doi:10.1029/2011JA016489

Roux, A., Robert, P., Fontaine, D., Contel, O. L., Canu, P., and Louarn, P. (2015). What is the nature of magnetosheath FTEs? *J. Geophys. Res. Space Phys.* 120, 4576–4595. doi:10.1002/2015JA020983

Runov, A., Sergeev, V. A., Baumjohann, W., Nakamura, R., Apatenkov, S., Asano, Y., et al. (2005). Electric current and magnetic field geometry in flapping magnetotail current sheets. *Ann. Geophys.* 23, 1391–1403. doi:10.5194/angeo-23-1391-2005

Runov, A., Sergeev, V. A., Nakamura, R., Baumjohann, W., Apatenkov, S., Asano, Y., et al. (2006). Local structure of the magnetotail current sheet: 2001 Cluster observations. *Ann. Geophys.* 24, 247–262. doi:10.5194/angeo-24-247-2006

Russell, C. T., Luhmann, J. G., and Strangeway, R. J. (2016). *Space physics: an introduction*. Cambridge: Cambridge University Press. doi:10.1017/9781316162590

Shen, C., and Dunlop, M. (2023). Field gradient analysis based on a geometrical approach. *J. Geophys. Res. Space Phys.* 128, e2023JA031313. doi:10.1029/2023JA031313

Shen, C., Dunlop, M., Ma, Y. H., Chen, Z. Q., Yan, G. Q., Liu, Z. X., et al. (2011). The magnetic configuration of the high-latitude cusp and dayside magnetopause under strong magnetic shears. *J. Geophys. Res. Space Phys.* 116, n/a-n/a. doi:10.1029/2011ja016501

Shen, C., and Dunlop, M. W. (2008). "Geometrical structure analysis of the magnetic field," in *Multi-spacecraft analysis methods revisited*. Editors G. Paschmann, and P. W. Daly (Noordwijk, Netherlands: ESA Communications Keplerlaan), 27–32.

Shen, C., Li, X., Dunlop, M., Liu, Z. X., Balogh, A., Baker, D. N., et al. (2003). Analyses on the geometrical structure of magnetic field in the current sheet based on cluster measurements. *J. Geophys. Res. Space Phys.* 108. doi:10.1029/2002ja009612

Shen, C., Li, X., Dunlop, M., Shi, Q. Q., Liu, Z. X., Lucek, E., et al. (2007). Magnetic field rotation analysis and the applications. *J. Geophys. Res. Space Phys.* 112. doi:10.1029/2005ja011584

Shen, C., Liu, Z. X., Li, X., Dunlop, M., Lucek, E., Rong, Z. J., et al. (2008a). Flattened current sheet and its evolution in substorms. *J. Geophys. Res. (Space Physics)* 113, A07S21. doi:10.1029/2007JA012812

Shen, C., Rong, Z. J., and Dunlop, M. (2012a). Determining the full magnetic field gradient from two spacecraft measurements under special constraints. *J. Geophys. Res. Space Phys.* 117. doi:10.1029/2012JA018063

Shen, C., Rong, Z. J., Dunlop, M. W., Ma, Y. H., Li, X., Zeng, G., et al. (2012b). Spatial gradients from irregular, multiple-point spacecraft configurations. *J. Geophys. Res. Space Phys.* 117. doi:10.1029/2012ja018075

Shen, C., Rong, Z. J., Li, X., Dunlop, M., Liu, Z. X., Malova, H. V., et al. (2008b). Magnetic configurations of the tilted current sheets in magnetotail. *Ann. Geophys.* 26, 3525–3543. doi:10.5194/angeo-26-3525-2008

Shen, C., Yang, Y. Y., Rong, Z. J., Li, X., Dunlop, M., Carr, C. M., et al. (2014). Direct calculation of the ring current distribution and magnetic structure seen by Cluster during geomagnetic storms. *J. Geophys. Res. Space Phys.* 119, 2458–2465. doi:10.1002/2013ja019460

Shen, C., Zhang, C., Rong, Z., Pu, Z., Dunlop, M. W., Escoubet, C. P., et al. (2021a). Nonlinear magnetic gradients and complete magnetic geometry from multispacecraft measurements. *J. Geophys. Res. Space Phys.* 126, e2020JA028846. doi:10.1029/2020JA028846

Shen, C., Zhou, Y., Gao, L., Wang, X., Pu, Z., Escoubet, C. P., et al. (2021b). Measurements of the net charge density of space plasmas. *J. Geophys. Res. Space Phys.* 126, e2021JA029511. doi:10.1029/2021JA029511

Shen, C., Zhou, Y., Ma, Y., Wang, X., Pu, Z., and Dunlop, M. (2021c). A general algorithm for the linear and quadratic gradients of physical quantities based on 10 or more point measurements. *J. Geophys. Res. Space Phys.* 126, e2021JA029121. doi:10.1029/2021JA029121

Shi, J., Guo, J., Dunlop, M., Zhang, T., Liu, Z., Lucek, E., et al. (2012). Inter-hemispheric asymmetry of dependence of the cusp location on dipole tilt during northward IMF conditions. *Ann. Geophys.* 30, 21–26. doi:10.5194/angeo-30-21-2012

Shi, J. K., Cheng, Z. W., Zhang, T. L., Dunlop, M., Liu, Z. X., Torkar, K., et al. (2010). South-north asymmetry of field-aligned currents in the magnetotail observed by Cluster. *J. Geophys. Res. Space Phys.* 115. doi:10.1029/2009JA014446

Shi, Q. Q., Tian, A. M., Bai, S. C., Hasegawa, H., Degeling, A. W., Pu, Z. Y., et al. (2019). Dimensionality, coordinate system and reference frame for analysis of in-situ space plasma and field data. *Space Sci. Rev.* 215, 35. doi:10.1007/s11214-019-0601-2

Shiokawa, K., Baumjohann, W., Haerendel, G., Paschmann, G., Fennell, J. F., Friis-Christensen, E., et al. (1998). High-speed ion flow, substorm current wedge, and multiple Pi 2 pulsations. *J. Geophys. Res. Space Phys.* 103, 4491–4507. doi:10.1029/97JA01680

Shore, R. M., Whaler, K. A., Macmillan, S., Beggan, C., Olsen, N., Spain, T., et al. (2013). Ionospheric midlatitude electric current density inferred from multiple magnetic satellites. *J. Geophys. Res. Space Phys.* 118, 5813–5829. doi:10.1002/jgra.50491

Tan, X., Dunlop, M. W., Dong, X. C., Yang, Y. Y., Du, Y. S., Shen, C., et al. (2023). Ring current morphology from MMS observations. *J. Geophys. Res. Space Phys.* 128. doi:10.1029/2023ja031372

Teh, W. L., Nakamura, T. K. M., Nakamura, R., Baumjohann, W., Russell, C. T., Pollock, C., et al. (2017). Evolution of a typical ion-scale magnetic flux rope caused by thermal pressure enhancement. *J. Geophys. Res. Space Phys.* 122, 2040–2050. doi:10.1002/2016JA023777

Trenchi, L., Kauristie, K., Käki, S., Vanhamäki, H., Juusola, L., Blagau, A., et al. (2020). "ESA field-aligned currents—methodology inter-comparison exercise," in *Ionospheric multi-spacecraft analysis tools*. Editors M. W. Dunlop, and H. Lühr (Springer), 167. doi:10.1007/978-3-030-26732-2_8

Vallat, C., Dandouras, I., Dunlop, M., Balogh, A., Lucek, E., Parks, G. K., et al. (2005). First current density measurements in the ring current region using simultaneous multi-spacecraft CLUSTER-FGM data. *Ann. Geophys.* 23, 1849–1865. doi:10.5194/angeo-23-1849-2005

Vogt, J., Albert, A., and Marghitu, O. (2009). Analysis of three-spacecraft data using planar reciprocal vectors: methodological framework and spatial gradient estimation. *Ann. Geophys.* 27, 3249–3273. doi:10.5194/angeo-27-3249-2009

Vogt, J., Paschmann, G., and Chanteur, G. (2008). "Reciprocal vectors," in *Multi-spacecraft analysis methods revisited*. Editors G. Paschmann, and P. W. Daly (Noordwijk, Netherlands: ESA Communications Keplerlaan), 33–46.

Vogt, J., Sorbalo, E., He, M., and Blagau, A. (2013). Gradient estimation using configurations of two or three spacecraft. *Ann. Geophys.* 31, 1913–1927. doi:10.5194/angeo-31-1913-2013

Wang, H., Ma, S. Y., Lühr, H., Liu, Z. X., Pu, Z. Y., Escoubet, C. P., et al. (2006). Global manifestations of a substorm onset observed by a multi-satellite and ground station network. *Ann. Geophys.* 24, 3491–3496. doi:10.5194/angeo-24-3491-2006

Wang, T., Alexandrova, O., Perrone, D., Dunlop, M., Dong, X., Bingham, R., et al. (2019). Magnetospheric multiscale observation of kinetic signatures in the Alfvén vortex. *Astrophysical J.* 871, L22. doi:10.3847/2041-8213/aafe0d

Wang, Z., Fu, H. S., Liu, C. M., Liu, Y. Y., Cozzani, G., Giles, B. L., et al. (2019). Electron distribution functions around a reconnection X-line resolved by the FOTE method. *Geophys. Res. Lett.* 46, 1195–1204. doi:10.1029/2018GL081708

Wang, Z., Fu, H. S., Vaivads, A., Burch, J. L., Yu, Y., and Cao, J. B. (2020). Monitoring the spatio-temporal evolution of a reconnection X-line in space. *Astrophysical J.* 899, L34. doi:10.3847/2041-8213/abad2c

Xiao, C., Liu, W., Shen, C., Zhang, H., and Rong, Z. (2018). Study on the curvature and gradient of the magnetic field in Earth's cusp region based on the magnetic curvature analysis method. *J. Geophys. Res. (Space Physics)* 123, 3794–3805. doi:10.1029/2017JA025028

Xiao, C. J., Pu, Z. Y., Ma, Z. W., Fu, S. Y., Huang, Z. Y., and Zong, Q. G. (2004). Inferring of flux rope orientation with the minimum variance analysis technique. *J. Geophys. Res. Space Phys.* 109. doi:10.1029/2004JA010594

Xiao, C. J., Wang, X. G., Pu, Z. Y., Ma, Z. W., Zhao, H., Zhou, G. P., et al. (2007). Satellite observations of separator-line geometry of three-dimensional magnetic reconnection. *Nat. Phys.* 3, 609–613. doi:10.1038/nphys650

Xiao, C. J., Wang, X. G., Pu, Z. Y., Zhao, H., Wang, J. X., Ma, Z. W., et al. (2006). *In situ* evidence for the structure of the magnetic null in a 3D reconnection event in the Earth's magnetotail. *Nat. Phys.* 2, 478–483. doi:10.1038/nphys342

Yang, Y. Y., Shen, C., Dunlop, M., Rong, Z. J., Li, X., Angelopoulos, V., et al. (2016). Storm time current distribution in the inner equatorial magnetosphere: THEMIS observations. *J. Geophys. Res. Space Phys.* 121, 5250–5259. doi:10.1002/2015ja022145

Yang, Y. Y., Shen, C., Zhang, Y. C., Rong, Z. J., Li, X., Dunlop, M., et al. (2014). The force-free configuration of flux ropes in geomagnetotail: cluster observations. *J. Geophys. Res. Space Phys.* 119, 6327–6341. doi:10.1002/2013ja019642

Yao, Z. H., Pu, Z. Y., Owen, C. J., Fu, S. Y., Chu, X. N., Liu, J., et al. (2014). Current reduction in a pseudo-breakup event: THEMIS observations. *J. Geophys. Res. Space Phys.* 119, 8178–8187. doi:10.1002/2014ja020186

Zhang, Q. H., Dunlop, M. W., Lockwood, M., Holme, R., Kamide, Y., Baumjohann, W., et al. (2011). The distribution of the ring current: cluster observations. *Ann. Geophys.* 29, 1655–1662. doi:10.5194/angeo-29-1655-2011

Zhang, Y. C., Shen, C., Liu, Z. X., Rong, Z. J., Zhang, T. L., Marchaudon, A., et al. (2013). Two different types of plasmoids in the plasma sheet: cluster multisatellite analysis application. *J. Geophys. Res. Space Phys.* 118, 5437–5444. doi:10.1002/jgra.50542

Zhang, Y. C., Shen, C., Marchaudon, A., Rong, Z. J., Lavraud, B., Fazakerley, A., et al. (2016). First *in situ* evidence of electron pitch angle scattering due to magnetic field line curvature in the Ion diffusion region. *J. Geophys. Res. Space Phys.* 121, 4103–4110. doi:10.1002/2016JA022409

Zhao, C., Russell, C. T., Strangeway, R. J., Petrinec, S. M., Paterson, W. R., Zhou, M., et al. (2016). Force balance at the magnetopause determined with MMS: application to flux transfer events. *Geophys. Res. Lett.* 43, 11941–11947. doi:10.1002/2016GL071568